Monthly Notices of the ROYAL ASTRONOMICAL SOCIETY

MNRAS **552,** 1–30 (2026) https://doi.org/10.1093/mnras/stag354

ALMA Central Molecular Zone Exploration Survey (ACES) – II. 3 mm continuum images

Adam Ginsburg [1], Daniel L. Walker [2], Ashley T. Barnes [3], Xing Lu [4,5], Álvaro Sánchez-Monge [6,7], Jaime E. Pineda [8], Marc W. Pound,[9] Pei-Ying Hsieh [10], Katharina Immer [3], Qizhou Zhang [11], Nazar Budaiev [1], Savannah R. Gramze [1], Desmond Jeff [1,12], Claire Cook,[13] Alyssa Bulatek [1], Elisabeth A.C. Mills [13], the ACES collaboration, John Bally [14], Laura Colzi [15], Pablo García [16,17], Jonathan D. Henshaw [18,19], Izaskun Jiménez-Serra [15], Ralf S. Klessen [11,20,21,22], Simon R. Dicker [23], Steven N. Longmore [18,24]★, Francisco Nogueras-Lara [3,25], Víctor M. Rivilla [15], Miriam G. Santa-Maria [1,26], Q. Daniel Wang [27], Fengwei Xu [28,29], Cara Battersby [30], Paul T. P. Ho [31], J. M. Diederik Kruijssen [24], Maya Petkova [32], Mattia C. Sormani [33], Robin G. Tress [34], Jennifer Wallace [30], J. Armijos-Abendaño [35], Lucia Armillotta,[36] N. Bijas [37], Rojita Buddhacharya [18], Laura A. Busch,[8] Natalie O. Butterfield [12], Mélanie Chevance [20,24], Samuel Crowe [38], Ana Karla Díaz-Rodríguez [2], Katarzyna M. Dutkowska [39], Rubén Fedriani [25], Christoph Federrath [40], Simon C. O. Glover [20], Qi-Lao Gu,[4] Rebecca J. Houghton [18], Yue Hu [41], Namitha Issac [4], Janik Karoly [42], Mark R. Krumholz,[40] Fu-Heng Liang [3,43], Sergio Martín [44,45], Farideh Mazoochi,[46] Xing Pan,[11,47,48] Dylan Paré,[49] Thushara G. S. Pillai [50], Denise Riquelme-Vásquez [51], Anika Schmiedeke [52], Yoshiaki Sofue [53], Volker Tolls [11], Gwenllian M. Williams [54], Suinan Zhang [4], Emily Moravec [52], Charles E. Romero [23], Brian S. Mason [12], John Orlowski-Scherer[23] and H. Perry Hatchfield [30]

Affiliations are listed at the end of the paper

Accepted 2026 February 4. Received 2026 February 4; in original form 2025 July 18

ABSTRACT

The ALMA Central Molecular Zone Exploration Survey (ACES) has mapped $\gtrsim$ 1000 square arcminutes at 3 mm towards the centre of our Galaxy. ACES provides the first large-scale, high-resolution ($\sim$ 2.5 arcsec) view of the central $\sim$ 200 parsecs of the Milky Way. In this work, we describe the continuum data processing and present the continuum data products. In the combined mosaic of 45 individual ALMA mosaics, the typical RMS noise achieved is $\sim$ 0.1 mJy per $\sim$ 2.5 arcsec beam, though there is a tail of substantially higher noise towards regions with bright continuum structure, especially around Sgr A$*$ and Sgr B2. In-band spectral indices are measurable for a small fraction of the brightest and most compact sources, enabling distinction between dust-dominated and free-free- or synchrotron-dominated sources. To recover emission on large angular scales, we present the GBT MUSTANG-2 Three millimetre Extended Nucleus Survey (TENS), a new 10 arcsec resolution survey of the CMZ, which we combine with the ACES image by feathering. To demonstrate the quality and reliability of the ACES data, we compare to previously published ALMA data obtained with higher resolution and sensitivity, finding overall good agreement with past results, but some disagreement towards the brightest sources.

Key words: Galaxy: centre – ISM: structure.

★ E-mail: s.n.longmore@ljmu.ac.uk

© The Author(s) 2026.
Published by Oxford University Press on behalf of Royal Astronomical Society. This is an Open Access article distributed under the terms of the Creative Commons Attribution License (https://creativecommons.org/licenses/by/4.0/), which permits unrestricted reuse, distribution, and reproduction in any medium, provided the original work is properly cited.

Downloaded from academic.oup.com/mnras/article/552/2/stag354/8875763 by Liverpool John Moores University user on 02 November 2026

1 INTRODUCTION

Galactic Centres act as the engines of galaxy evolution, funnelling gas inward, converting it to stars and expelling it through energetic feedback (e.g. S. Veilleux, G. Cecil & J. Bland-Hawthorn 2005). Because the Milky Way's Central Molecular Zone (CMZ) is the only nucleus where these mechanisms can be spatially resolved from global ($>$ 100 pc) to star-forming (0.05 pc) scales and below, it is the benchmark for understanding nuclear star formation, stellar feedback, and the feeding of central supermassive black holes (e.g. R. Genzel, F. Eisenhauer & S. Gillessen 2010; S. N. Longmore et al. 2013; Event Horizon Telescope Collaboration 2022; J. D. Henshaw et al. 2023). Paradoxically, despite its dense reservoir of molecular gas, the CMZ is presently forming stars an order of magnitude more slowly than empirical relations predict (e.g. A. T. Barnes et al. 2017) and appears to do so episodically, perhaps regulated by turbulence and orbital dynamics (J. M. D. Kruijssen et al. 2014; M. R. Krumholz, J. M. D. Kruijssen & R. M. Crocker 2017; M. C. Sormani et al. 2020). A decisive explanation requires a contiguous, high-resolution census of where the dense gas – and the young stars it spawns – actually reside within the CMZ.

Conducting such a census is hampered by the fact that the CMZ is hidden behind the Galactic plane, rendering it effectively invisible at short (optical) wavelengths. It has been surveyed extensively at all other wavelengths, including X-ray (Q. D. Wang, E. V. Gotthelf & C. C. Lang 2002; M. P. Muno et al. 2009; V. Heard & R. S. Warwick 2013), near-infrared (e.g. Q. D. Wang et al. 2010; F. Nogueras-Lara et al. 2018), far-infrared (S. Molinari et al. 2011), millimetre (J. Bally et al. 2010; A. Ginsburg et al. 2013; J. E. Aguirre et al. 2011; Y. Tang et al. 2021b; Y. Tang, Q. D. Wang & G. W. Wilson 2021a; C. Battersby et al. 2020; M. W. Pound & F. Yusef-Zadeh 2018), and radio (C. J. Law, F. Yusef-Zadeh & W. D. Cotton 2008b; C. J. Law et al. 2008a; I. Heywood et al. 2022). However, at millimetre wavelengths, the spatial resolution, coverage, and sensitivity have been limited before ALMA.

The ALMA Central Molecular Zone Exploration Survey (ACES) continuum mosaic presented here aims to provide a contiguous, high-resolution census of dense gas and young high-mass stars throughout the CMZ. ALMA's small native field-of-view means that mosaicking is required to cover areas larger than about an arcminute square. While mosaicking is a well-established technique, it adds a significant layer of complexity to the image processing, both stretching the approximations used in interferometric imaging (R. D. Ekers & A. H. Rots 1979; T. J. Cornwell 1988; J. Pety & N. Rodríguez-Fernández 2010) and the limits of computing hardware. While previous works have covered substantial areas, spanning 10's of square arcminutes (e.g. A. Ginsburg et al. 2022; A. K. Leroy et al. 2021), ACES enters new territory by imaging a mosaic-of-mosaics spanning 45 individual fields and $>$ 1000 square arcminutes.

In this work, we present the continuum data processing approach for the largest mosaic the ALMA 12 m array has yet produced, which resulted in additional technical challenges not faced by smaller mosaics-of-mosaics. Covering >1000 arcmin^2 with $\sim$2.5 arcsec (0.05 pc) resolution and $\sim$0.1 mJy beam^{-1} sensitivity (detailed explanation of these values is in Section 3), the ACES 3 mm map (augmented with MUSTANG-2 to recover >3 arcmin scales; see Section 2.1) supplies column-density and spectral-index information across the CMZ. By mapping the locations of compact dust cores, H II regions and synchrotron emission, these data are pivotal to the ACES science objectives of building a global understanding of star formation, feedback, and the mass flows and energy cycles across the CMZ.

This paper presents the continuum images from ACES. It is accompanied by an overview paper describing the aims of the project (S. N. Longmore & ACES Team 2025) and three papers describing the cubes in high-resolution (D. Walker & ACES Team 2025), medium-resolution (X. Lu & ACES Team 2025), and low-resolution (P.-Y. Hsieh & ACES Team 2025) spectral windows.

This paper presents a summary of the observations in Section 2, a detailed description of the data processing and results in Section 3, and a brief set of analyses to validate the data in Section 4. We conclude with a brief summary.

2 OBSERVATIONS

Observations in the ACES project were performed in the ALMA Large Program 2021.1.00172.L (S. N. Longmore & ACES Team 2025). ACES used a hybrid spectral window set-up, in which two narrow-band windows focused on high-resolution spectral line observations, two medium-band windows compromised between spectral resolution and coverage, and two broad-band windows provide the majority of the continuum sensitivity. The spectral set-up is summarized in Table 1. The 12 m array observations, which are those discussed here (see Section 3.7 for discussion of short spacing recovery), were carried out in configurations C-3 and C-4 with start dates between January 1 and 2022 September 30.[1] A table in the appendix, Table B1, reports the full details of these observations, including the field name, time of each execution, the configuration, the precipitable water vapour (PWV) during the execution, the number of pointings in the scheduling block, the exposure time per mosaic pointing, and the expected resolution and largest angular scale.

The ACES observations included data from the 7 m ACA array, however, we do not present them here. While the 7 m array data fill in the short spacing to some degree, the longest baselines of the 7 m array (45 m) are smaller than the 100 m diameter of the Green Bank Telescope, and there are no ALMA total power (TP) continuum data. The MUSTANG-2 MGPS90 data (Section 2.1) have significantly better angular scale recovery and noise characteristics on the overlap scales; see Fig. 1. The 7 m data require additional reprocessing and reimaging that we opted not to do for this paper. The only use case for which the 7 m continuum data would be preferred is spectral index measurement on larger angular scales (see Section 4.1). The other ACES data papers that present images of the line data will include the 7 m and TP data (D. Walker & ACES Team 2025; X. Lu & ACES Team 2025; P.-Y. Hsieh & ACES Team 2025).

The final continuum images from ACES and the feathered ACES plus TENS (see Section 2.1) data are shown in Section 3.7. These images, and the process of producing them, will be discussed in Section 3. The labelling scheme for the fields is given in Fig. 2.

The (u, v) coverage of ACES was planned to be as uniform as possible. However, as a particularly large Large Program, it was necessary to spread ACES observations over several array configurations. The resulting (u, v) coverage is not uniform, as can be seen in Fig. 3. For example, field b has significantly more

[1] https://almascience.eso.org/observing/observing-configuration-schedule/prior-cycle-observing-and-configuration-schedule

Downloaded from academic.oup.com/mnras/article/552/2/stag354/8875763 by Liverpool John Moores University user on 02 November 2026

Table 1. ACES Spectral Configuration.

SPW	ν_L GHz	ν_U GHz	$\Delta\nu$ MHz	Bandwidth GHz	Lines
25	85.9656	86.4344	0.4880	0.46875	$HC^{15}N$ 1-0, SO 2(2)-1(1), SiO 2-1 v=1 maser, $H^{13}CN$ 1-0 86.05496, 86.09395, 86.24337, 86.33992
27	86.6656	87.1344	0.4880	0.46875	$H^{13}CO+$ 1-0, SiO 2-1, $HN^{13}C$ 1-0 86.7543, 86.84696, 87.09085
29	89.1592	89.2178	0.061030	0.05859	HCO+ 1-0 89.18852
31	87.8959	87.9545	0.061030	0.05859	HNCO 4-3 87.925238
33	97.6625	99.5375	0.97656	1.875	CS 2-1, CH_3CHO 5(1,4)-4(1,3) A-, H40α, SO 3(2)-2(1) 97.98095, 98.90095, 99.02295, 99.29987
35	99.5625	101.438	0.97656	1.875	HC_3N 11-10 100.0763

Note. ACES Spectral Configuration, including a non-exhaustive list of prominent, potentially continuum-affecting, lines. The included lines are those that are, in at least some portion of the survey, masked out (see Section 3.5). The rest frequencies of the targeted lines are given in GHz in the row below their names. The columns ν_L, ν_U, and $\Delta\nu$ are the lower frequency, upper frequency, and frequency resolution, respectively.

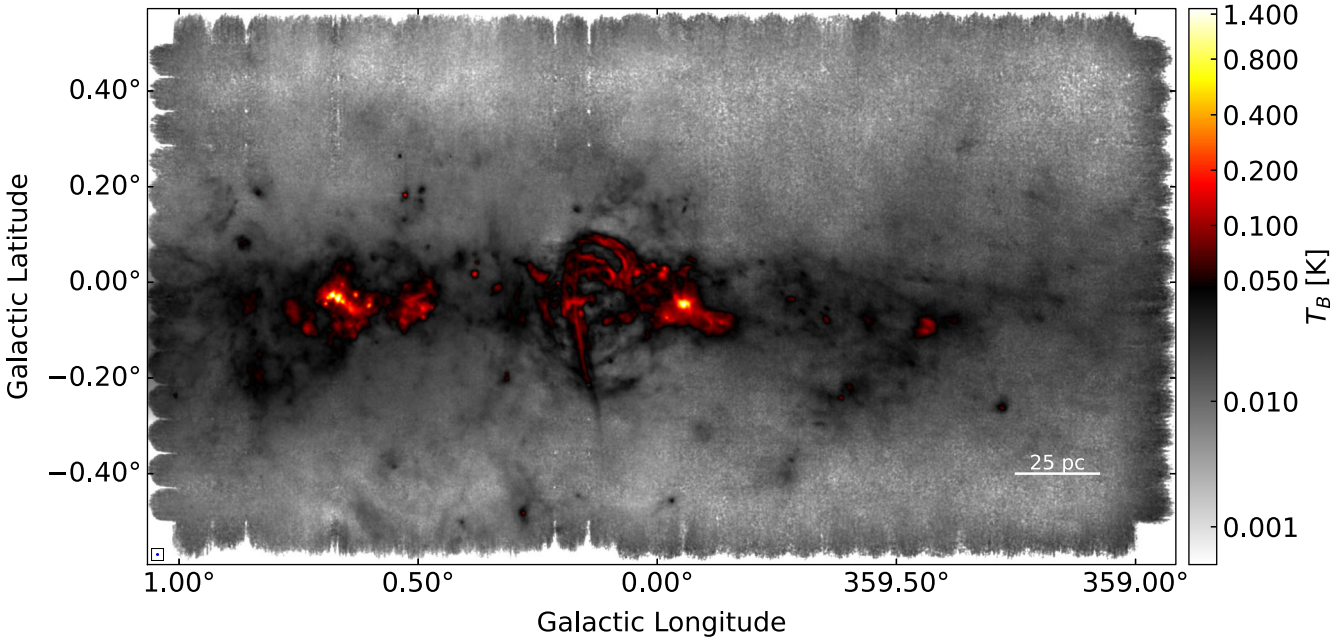


Figure 1. The GBT MUSTANG-2 TENS image combined with Planck all-sky data that is used to fill in the short spacings missing in the ALMA interferometric data.

baselines at larger separation than field c. The effect of this varying (u, v) coverage will be discussed in Section 3.4.

2.1 GBT mustang-2 TENS

The ACES data, as with all interferometric observations, lack short spacing continuum information. While the 7 m ACA array is intended to provide shorter spacings than the 12 m array, its (u, v) coverage is only marginally better, with shortest baselines $\sim$ 10m corresponding to largest angular scales $\sim$ 60 arcsec. In order to improve on this largest angular scale limit, we obtained single-dish data using the Green Bank Telescope's MUSTANG-2 instrument (S. R. Dicker et al. 2014), which is a 215-element bolometer array with a bandpass spanning 75–105 GHz.

We used data from the MUSTANG-2 Galactic Plane Survey (MGPS90; A. Ginsburg et al. 2020) and the new TENS (Three millimetre Expanded Nucleus Survey, which we present here) continuum images. The GBT's dish diameter of 100 m overlaps well with the ALMA 12 m array's short baselines (see Fig. 3 and Section 3.4). The data reduction process, and half of the data, are described in A. Ginsburg et al. (2020). The final data product was feathered with Planck all-sky data to fill in the short spacing in the GBT MUSTANG-2 data, which is required because bolometric data processing applies a high-pass filter that behaves similarly to interferometric filtering.

The MUSTANG-2 Galactic Plane Survey only covered $\ell \gtrsim -0.1$, which left half the ACES footprint unobserved. We therefore acquired additional GBT observations on 2024 May 2, which covered the right half of the ACES footprint, under the TENS program. The full area covered by TENS is $|\ell| < 1$, $|b| < 0.5$ The MUSTANG-2 beam shape and variations in the instrument response were measured every 30 min using observations of

Downloaded from academic.oup.com/mnras/article/552/2/stag354/8875763 by Liverpool John Moores University user on 02 November 2026

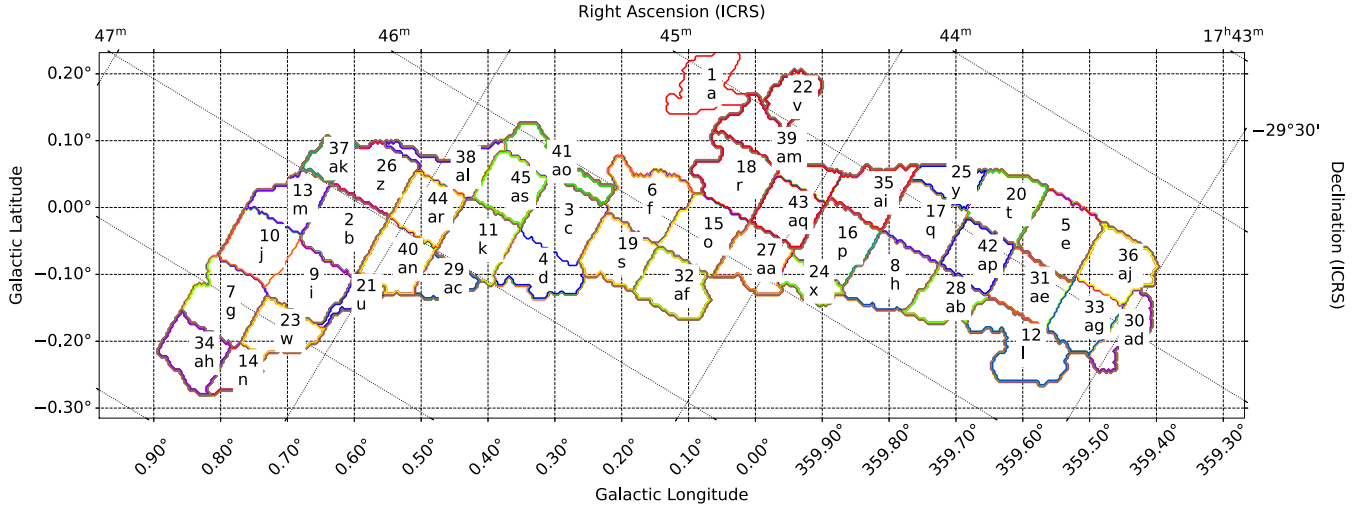


Figure 2. Overview of the ACES fields. The survey footprint is comprised of 45 mosaics, labelled `a` through `as` (1 through 45). The mapping from letters to Galactic coordinates can be found in Table B1.

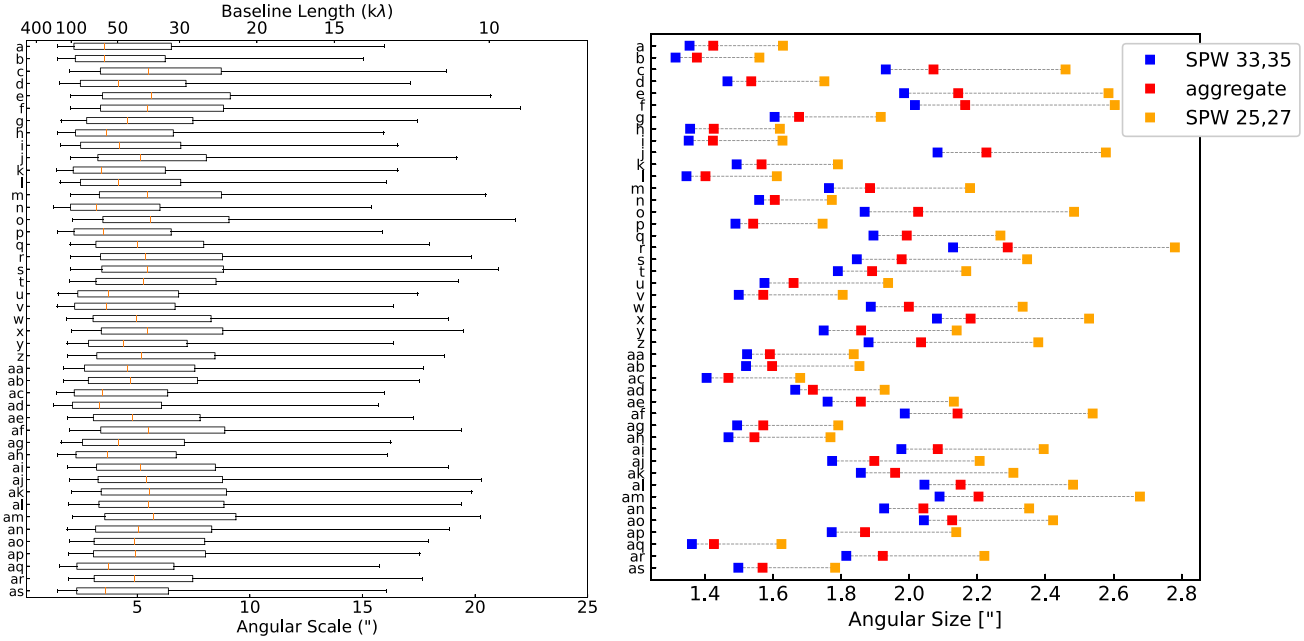


Figure 3. Visualization of the (u, v) coverage per field. Left: The box-and-whisker plots in each row show the 5th and 95th percentile as whiskers and the 25th and 75th percentile as box ends. The field identifiers listed on the left side of the plot refer to the labels shown in Fig. 2. Right: The beam geometric average sizes for each image product, in arcseconds, for each imaged field. The points show the high-frequency spectral windows, the aggregate bandwidth image including all spectral windows, and the low-frequency spectral windows in blue, red, and orange, respectively, from left to right.

the nearby radio source J1700-2610. At the beginning and end of each observation session, the amplitude of this source was tied to multiple ALMA flux calibrators (extrapolated to match MUSTANG-2's bandpass). The relative elevation of the sources and the opacity calculated from archival weather data were also used to give a calibration accuracy better than 10 per cent. The calibrated timestreams were then used with the Minkasi[2] maximum likelihood mapmaker. As some areas of the map are signal-dominated, multiple iterations were used with the positive flux from the previous step being subtracted from the raw data before re-estimating the noise.

Further processing of these data, and their combination with the ACES data, are described in Section 3.7.

3 DATA PROCESSING

We use CASA for calibration and imaging (CASA Team et al. 2022). All of the calibration was performed using the appropriate CASA version specified in the ALMA archive data set. We ran the `scriptForPI.py` file for each measurement observation unit set (MOUS), i.e. we did not perform any custom calibration.

[2] https://github.com/sievers/minkasi

Downloaded from academic.oup.com/mnras/article/552/2/stag354/8875763 by Liverpool John Moores University user on 02 November 2026

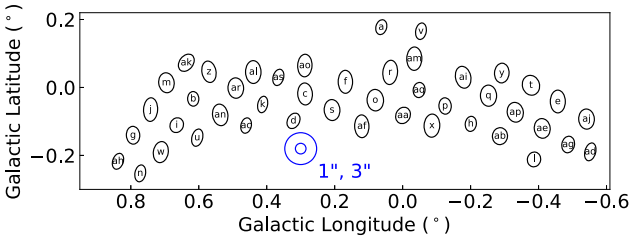


Figure 4. Map of the aggregate-resolution beam relative sizes and orientations by field. Each ellipse has major and minor diameter proportional to the full-width half-max (FWHM) of the corresponding beam. The concentric blue circles at the bottom-centre show the size scale to associate with the beams; they have diameters of 1 and 3 arcsec (the beams are not shown to scale with respect to the axis labels).

Table 2. Continuum image products.

Image Name	SPWs	Beam
Low, circular	25, 27	2.80 arcsec
High, circular	33, 35	2.14 arcsec
All data, circular	25, 27, 33, 35	2.30 arcsec
All data, best resolution	25, 27, 33, 35	n/a

For most of the ACES data, this was version `6.2.1.7`, but a few fields required reprocessing or were obtained in a later cycle and were calibrated with `6.4.1.12`. However, at later stages, we used `6.5.5-21`; the versions used for imaging are reported in the FITS header under the `ORIGIN` keyword.

3.1 Data quality assessment

We performed additional quality assessment, on top of ALMA's QA0 and QA2 processes, to check each scheduling block. Our assessment included a thorough inspection of the weblogs (the web pages produced by the ALMA pipeline for visual inspection) and interactive exploration of the delivered image products. Downloading and unpacking of the weblogs was handled automatically by the ACES pipeline, and links were created to github issues, one per scheduling block. The issues can be found on github at https://github.com/ACES-CMZ/reduction_ACES/issues, with each window labelled by its unique identifier (UID), the ACES field name (Fig. 2), and the array name. The full history of our team's analysis of each scheduling block can be found on those Issue pages.

3.2 Imaging

We imaged individual mosaic fields using parameters drawn from the ALMA pipeline. All fields were reimaged. The pipeline automatically selected parameters that are often user selected, such as the number of pixels, cell size, number of iterations, and threshold.[3] We adopted the automated pipeline parameters for all cases where they were available and the manual imaging parameters otherwise, increasing `cyclefactor` in only a few cases (`ag`, `i`, `aa`, and `z`) to improve convergence of the clean. The robust parameter adopted for each field was 0.0, 0.5, or 1.0, as listed in Table C1; these are determined by the heuristic pipeline to optimize the noise and beam size. We investigated changing robust parameter for the fields with the largest beams, but found no significant improvement, as these were already imaged with a low robust parameter (small beam). The complete set of parameters used to image each field can be found using the `merge_tclean_commands.py` script on the imaging code github repository.[4]

3.3 Mosaic image products

The ACES data span a frequency range of 86−102 GHz, such that the frequency range $(\nu_{max} - \nu_{\rm min})/\nu_{\rm max} = 16$ per cent, which means the low- and high-frequency ends of the band have appreciably different central frequencies and therefore effective beam sizes (see Section 3.5). We therefore produce several different continuum mosaic images: one including all continuum-containing windows, one including only the low frequencies ($<$ 87 GHz, spw 25, and 27), and one including only high frequencies ($>$ 98 GHz, spw 33, and 35). Additionally, we produce a mosaic of the images in their native resolution: this image should not be used for quantitative measurements, since it has inconsistent units (Jy beam^{-1}, but the beam size varies); instead, it is distributed so that those interested in the highest resolution views ACES can provide are able to quickly examine the data. The beam sizes in this final image are shown in Fig. 4. All of these images are produced with the same measurement sets, i.e. the 12 m array data.

Because of the differing beam size, the overall footprint of ACES is slightly frequency-dependent. The total areal coverage of the ACES 12 m data images is 1286 arcmin^2 at the low-frequency end, covering spectral windows 25 and 27, and 1261 arcmin^2 for the high-frequency window (33, 35). The 7 m array mosaic (not presented here) covers a slightly larger area.

All of the science-usable mosaic file names contain the string `continuum_commonbeam_circular_reimaged`. The 12 m data use three suffixes, `mosaic`, `spw25_27_mosaic`, and `spw33_35_mosaic`, referring to thee rows of Table 2. Additionally, we provide a file `12m_continuum_reimaged_mosaic.fits` that is a mosaic of each of the fields imaged at their native resolution. It is provided as a finder chart for the highest resolution data. This image should not be used for measurements because it has inconsistent resolution across the field of view.

3.4 Angular resolution & beams

The ACES program as proposed aimed to achieve a uniform beam size of 1.5 arcsec with a noise level of 0.13 mJy beam^{-1}. Because of the limitations noted in Section 2, this goal was not achieved. ALMA's Quality Assessment Phase 2 (QA2) process allows for observations to be accepted and passed to the PI if the noise is within 10 per cent and the geometric average of the beam axes at the representative frequency of 100.5 GHz is within 20 per cent of the target.[5] Fig. 5 shows that all of the observations using the high-frequency data fell within the 20 per cent target of 1.8 arcsec

[3]Except for two fields, `al` and `am`, which were manually imaged by the ALMA observatory.

[4]https://github.com/ACES-CMZ/reduction_ACES

[5]https://help.almascience.org/kb/articles/what-are-the-current-qa2-requirements

Downloaded from academic.oup.com/mnras/article/552/2/stag354/8875763 by Liverpool John Moores University user on 02 November 2026

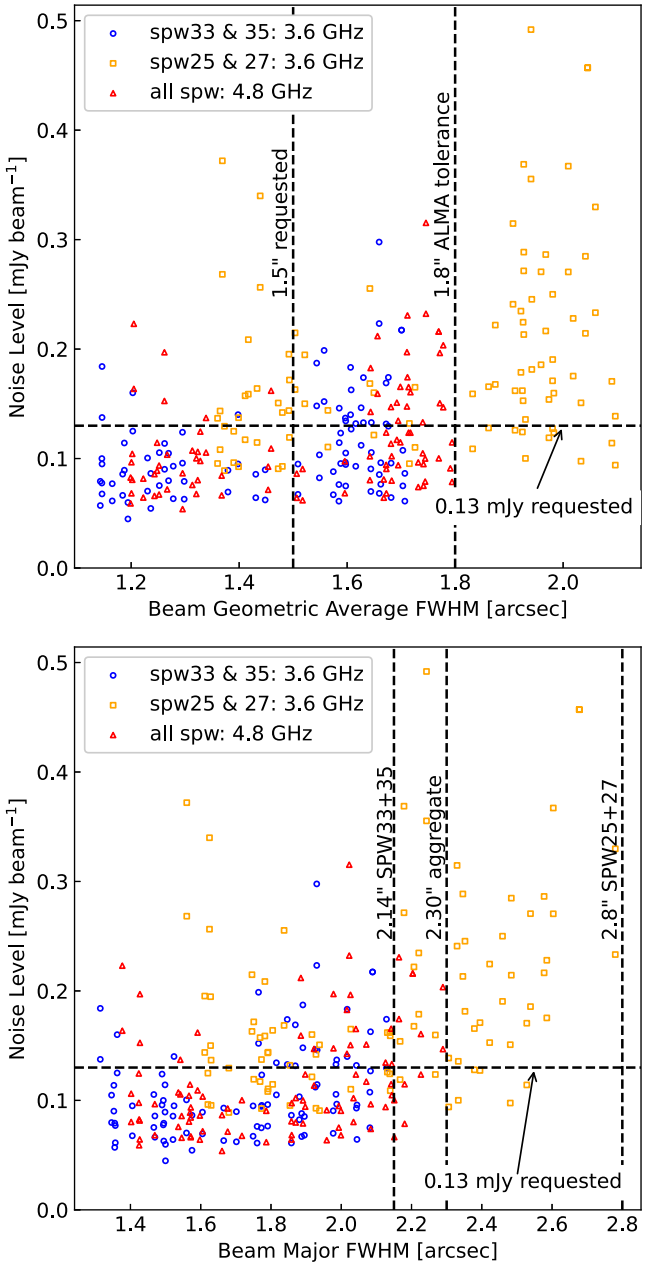


Figure 5. Noise vs beam size for each field. The plotted beam size is the geometric average between the major and minor axes (top) and the major axis size (bottom). The noise is the MAD-estimated standard deviation.

using the geometric average (the noise axis will be described in Section 3.6).

The effective resolution of the ACES maps is set by the largest beam major axis, not the geometric average. A uniform map of the full mosaic is needed to provide a consistently interpretable image of the CMZ. The common beam we adopt is the smallest circular beam that encompasses all synthesized beams. The resulting beam sizes in the combined mosaics are given in Table 2. The beam size for each field can be seen in Table C1; field `am` sets the limiting resolution, though field `r` has the largest geometric average beam size.

3.5 Continuum selection

The continuum selection was originally performed automatically by the ALMA pipeline. It resulted in different amounts of bandwidth being included in each field. Fig. 6 (top) shows the selection as a function of frequency and field number.

However, during our QA process, we discovered that significant bandwidth was being unnecessarily excluded and, particularly in the two narrow windows (spw29 & 31), some contamination was included. We therefore recalculated the continuum selection using a process based on Á. Sánchez-Monge et al. (2018). We used the fully imaged spectral cubes, which will be described in companion papers (D. Walker & ACES Team 2025; X. Lu & ACES Team 2025; P.-Y. Hsieh & ACES Team 2025). For each cube, we:

(i) Calculate the peak intensity spectrum, i.e. the brightest pixel in each channel.

(ii) Calculate the median and the standard deviation estimated from the median absolute deviation ($\sigma_{\rm MAD}$)[6] of the peak intensity spectrum.

(iii) Select pixels as continuum if their values in the peak intensity spectrum are within $\pm 2.5\sigma_{\rm MAD}$ of the median.

(iv) Remove isolated continuum selections by running two iterations of binary erosion[7] followed by one iteration of binary dilation.[8]

The resulting selections, shown in the lower panel in Fig. 6, are more consistent between fields than the ALMA pipeline selection. The new selections generally include more bandwidth, and therefore the reprocessed images presented here have higher sensitivity than the archive products.[9] Fig. 7 summarizes the resulting amount of bandwidth included in each field.

These continuum selections result in a variety of different effective central frequencies ($\nu_{\rm obs}$) for the image products described above (Section 3.3). The upper and lower frequency images each are nearly monochromatic, independent of the spectral index of the input source. However, the aggregate bandwidth image has a $\nu_{\rm obs}$ that depends on the input spectral index. The resulting intensity-weighted average frequency $\nu_{\rm obs}$, given by equation

$$\nu_{\rm obs} = \frac{\int_{\rm obs} \nu^\alpha \nu d\nu}{\int_{\rm obs} \nu^\alpha d\nu} \quad (1)$$

where α is the spectral index ($\alpha = 2$ corresponds to the Rayleigh–Jeans tail of a blackbody) and the subscript *obs* indicates that the integral is limited to the observed wavelengths included in the continuum, is given in Table 3.

3.6 Noise maps

We perform noise estimation by locally measuring the RMS in the continuum images. We operate directly on the images, not the residuals, since the CLEAN algorithm can potentially remove noise from the residual. The noise we estimate is appropriate for the beam scale, but is not appropriate for larger angular scales.

[6] $\sigma_{MAD} = 1.4286$ MAD if the distribution is Gaussian. We use the astropy `mad_std` function.
[7] https://docs.scipy.org/doc/scipy/reference/generated/scipy.ndimage.binary_erosion.html
[8] https://docs.scipy.org/doc/scipy/reference/generated/scipy.ndimage.binary_dilation.html
[9] https://almascience.org/aq/

Downloaded from academic.oup.com/mnras/article/552/2/stag354/8875763 by Liverpool John Moores University user on 02 November 2026

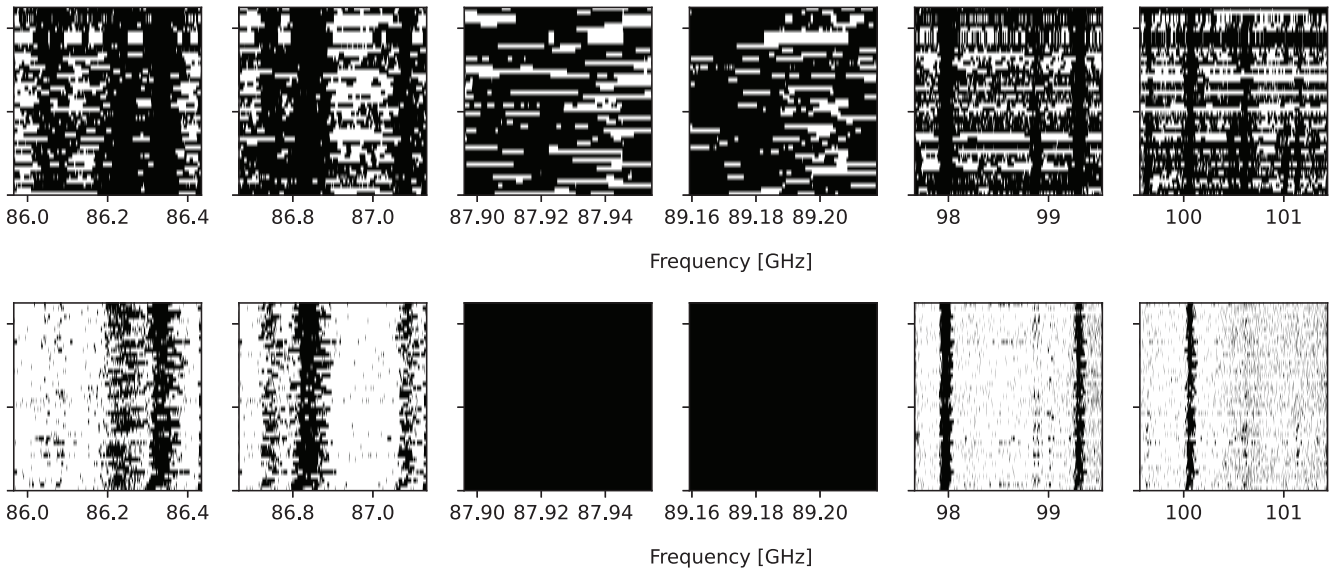


Figure 6. Continuum selection for the 12 m data before (top) and after (bottom) re-estimation of the continuum selection as a function of field number (vertical) and frequency (horizontal). These figures give a visual indication of the amount of bandwidth recovered with the `statcont`-based continuum selection. It also shows that the field-to-field variation is greatly reduced using the improved approach. Fig. 7 labels the fields in the same order as shown here; field labels are omitted in this figure because they would be too small. Black regions are those identified as emission line contaminated and are not used for continuum measurement; the middle two windows are entirely excluded as they have line emission at all frequencies. Note that the rightmost two panels comprise the majority of the total bandwidth, as the X-axes are not on the same scale.

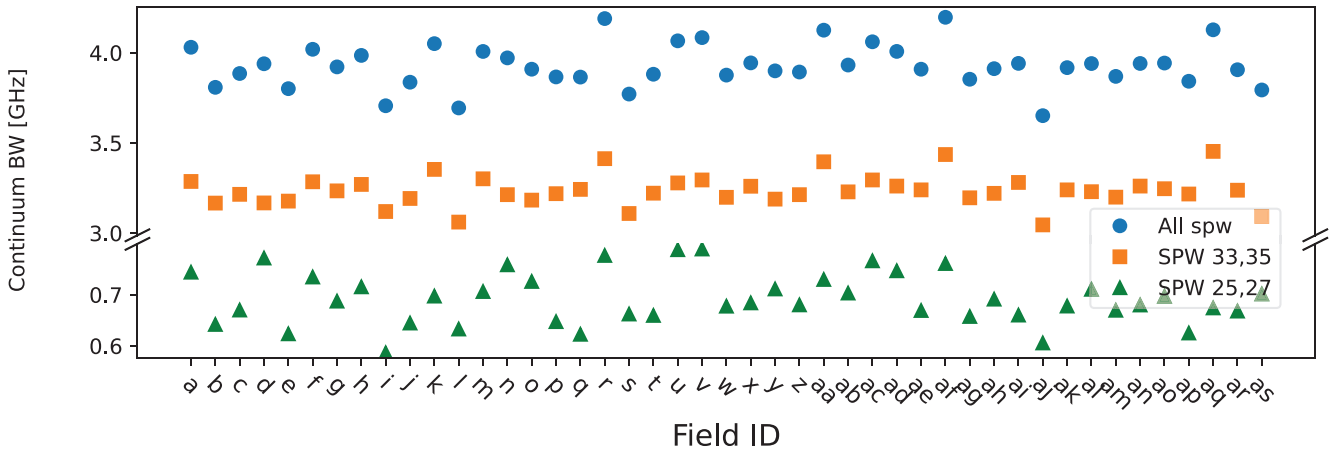


Figure 7. Continuum bandwidth used for continuum mapping versus field number. The three colours show the aggregate over all frequencies (blue circles), spectral windows 33+35 (orange squares), and spectral windows 25+27 (green triangles), from top to bottom, respectively. Note that spectral windows 25+27 are smaller than 33+35, so the *y*-axis label is split.

Table 3. Effective central frequencies.

α	$\nu_{\rm eff,agg}$ GHz	$\nu_{\rm eff,33+35}$ GHz	$\nu_{\rm eff,25+27}$ GHz
-2	96.674	99.519	86.536
-1	96.984	99.531	86.537
0	97.271	99.543	86.539
1	97.535	99.555	86.541
2	97.775	99.567	86.542
3	97.994	99.579	86.544
4	98.193	99.591	86.546

Note. This table reports the effective central frequency (equation 1) for assumed power-law flux indices α for the aggregate (subscript agg), high-frequency (SPW 33+35), and low-frequency (SPW 25+27) windows.

Scales somewhat larger than the beam generally will have lower noise, since they are sampled with the same (u, v) spacing used to produce the synthesized beam, while those much larger than the beam will have progressively greater uncertainty because they are more sparsely sampled. The noise level is roughly set by the (u, v) coverage (see Fig. 3), but must be empirically measured at any given scale.

The noise estimation technique we adopt minimizes the contribution of point sources to the noise, but accounts for the increased uncertainty produced by the presence of structured extended emission. We measure the local RMS weighted with a Gaussian with width three times that of the beam major axis.

$$RMS_j^2 = \Sigma_i \left[(I_i - \bar{I}_j)^2 K_i\right] \quad (2)$$

Downloaded from academic.oup.com/mnras/article/552/2/stag354/8875763 by Liverpool John Moores University user on 02 November 2026

where K_i is a normalized Gaussian kernel, I_i is the intensity value at a given pixel, $\bar{I}_j$ is the local mean intensity value estimated using the same kernel, and the subscripts i and j are indices of individual pixels (the evaluation is carried out in two dimensions, but we write the one-dimensional form here for simplicity). This calculation is implemented in the `imaging.make_mosaic.rms_map` function in the ACES pipeline. To remove the contribution of point sources, we iteratively mask out pixels with surface brightness values $S_\nu > 2.5\sigma$ and then recompute σ until no more significant pixels are identified.

In detail, the process is:

(i) Create a smoothed image `sm` by convolving the image with a Gaussian kernel with width three times that of the beam.
(ii) Create a residual image from the original image minus the smoothed, `res = im - sm`.
(iii) Create a variance map by squaring the residual, `var = res`^{2}.
(iv) Compute the average variance over a three beam width area by convolving the variance map with the same Gaussian kernel.
(v) Compute the RMS as the square root of the variance map, σ =`var_sm`$^{1/2}$.
(vi) Mask out pixels with values in the original image greater than 2.5σ.
(vii) Repeat the above steps until no additional pixels are added to the mask.

The convolution steps ignore masked pixels using ASTROPY's convolve functions.

The resulting noise maps are shown in Fig. 8, and their histograms in Fig. 9.

The noise is remarkably higher in a few regions. Most significantly, both Sgr A ($\ell \sim -0.05, b \sim -0.05$) and Sgr B2 ($\ell \sim 0.68, b \sim -0.01$) have dramatically higher noise because of bright, challenging-to-clean, structure. Both of these regions would require substantial self-calibration to reduce their noise and increase their dynamic range, but past experience suggests the noise would still remain highly elevated because of the multiscale extended structure (A. Ginsburg et al. 2018). Sgr A also contains the highly variable point source Sgr A$*$, which is not well-modelled by a single flux value. We chose not to attempt significantly deeper cleaning of these regions for this publication, in part because comparable or superior images within these high-noise areas have alreadybeen published (Sgr B2; A. Ginsburg et al. 2018, see also Section 4.2.1) or because we have not yet determined an appropriate path towards high-dynamic range imaging (Sgr A$*$).

The remaining high-noise areas are less extreme and simply follow extended structure: this extended structure contributes to the measured RMS, and while its presence limits our ability to identify point sources, it is not truly noise. One feature that drives the highly structured noise is the penultimate step in the above process, in which only positive pixels are masked out. Negative bowls surrounding bright extended structures contribute to the RMS estimate and are not masked out. There is one apparently low-noise region at the top of field v in the spw33+35 maps: the signal in this region has spuriously been suppressed, and we have been unable to diagnose the issue; data in this region of the spw33+35 mosaic image should not be used. No other regions were so affected, and it is clear that only one spectral window is affected in this particular case.

For individual fields, we present a simple summary statistic rather than a map. We compute $\sigma_{\rm MAD}$ for each field in their native Jy beam^{-1} unit. The field-by-field noise is summarized in Fig. 5, where it is shown as a function of beam size. The noise in each field is a function of both integration time and cleaning depth.

3.7 Single dish combination

We merge our images with the MUSTANG-2 Galactic Plane Survey (MGPS90) and TENS (Three millimetre Expanded Nucleus Survey) continuum images. The data are described in Section 2.1; here, we discuss the combination with different scales.

The MUSTANG-2 data are themselves insensitive to scales larger than ~ 3 arcmin, so to compensate for the missing large scales, we combine the MUSTANG-2 images with Planck all-sky images (Planck Collaboration I 2014).

We combine the ACES aggregate circular beam image with the MGPS90 image. We adopt a central frequency 97.3 GHz for the ACES data and 87.9 GHz for the MGPS90 data; these frequencies correspond to an assumed spectral index $\alpha = 0$, and in adopting that assumption, no scaling of the amplitudes is needed, but steep-index sources ($\alpha > 0$) will have mismatched large- and small- angular scale fluxes (see Section 4.1 for measurements of α). Before combination, we realigned the MGPS90 image to the ACES data using the `image_registration` package's `chi2_shift` tool.[10] We first convolved the ACES data to the MGPS90 resolution. We found that the MGPS90 data are offset by $\mathrm{d}\ell = -1.0$, $\mathrm{d}b = 2.98$ arcseconds from the ACES data. We therefore shift the MGPS90 data before combining, and we record this offset in the `SHIFTED` header keyword. The data are combined using the feathering technique (W. D. Cotton 2017) as implemented in the UVCOMBINE package in the `radio-astro-tools` suite.[11] The combined image has the same point spread function (PSF) as the interferometric image, i.e. the synthesized beam, since the synthesized beam is the reconstructed response of a filled aperture to a point source (see U. Rau, N. Naik & T. Braun 2019 for caveats about feathering). Unlike joint deconvolution, because the feathering is performed after cleaning, it has no effect on the shape of the fitted synthesized beam.

The ACES 12 m-only image and the feathered, combined image are shown in Fig. 10. We compare the before and after side by side in Fig. 11.

4 ANALYSIS

We perform some additional minimal analysis of the data to demonstrate the possibilities, and limitations, of the ACES data.

4.1 Spectral index

As noted in Section 3.3, the fractional bandwidth from the low end to the high end of the ACES band is ~ 16 per cent, which is enough to allow an in-band spectral index measurement in some cases. The radio spectral index α is defined such that

$$\frac{S_1}{S_2} = \left(\frac{\nu_1}{\nu_2}\right)^{\alpha} \quad (3)$$

[10] https://image-registration.readthedocs.io/en/latest/image_registration.html
[11] https://github.com/radio-astro-tools/uvcombine

Downloaded from academic.oup.com/mnras/article/552/2/stag354/8875763 by Liverpool John Moores University user on 02 November 2026

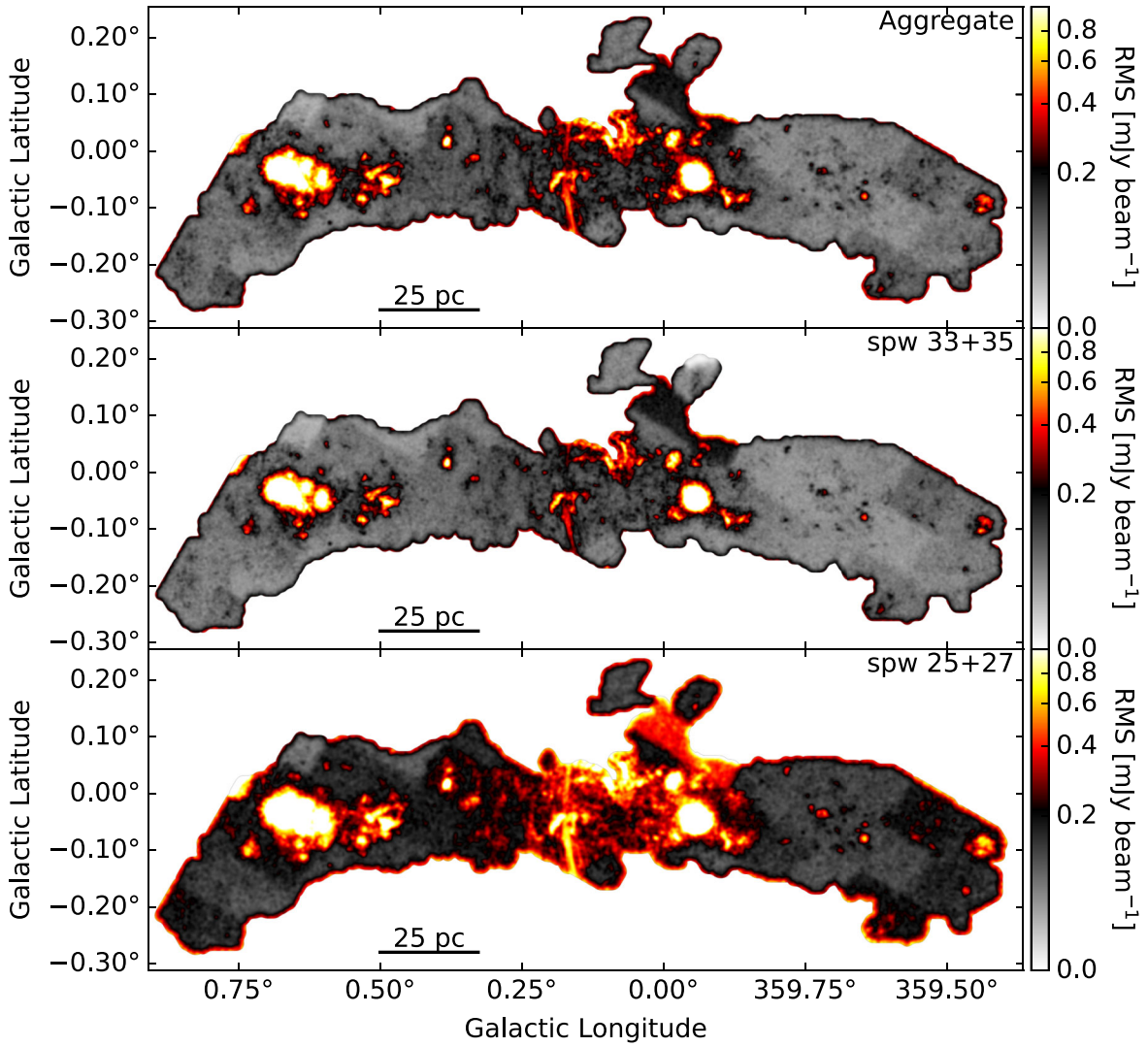


Figure 8. RMS maps. Top is full bandwidth, middle is spw25+27, bottom is spw33+35. Colourbar units are mJy beam^{-1}. Contours are shown at [10, 15, 20, 25, 30] mJy beam^{-1}.

Our images were produced with CASA's multiterm, multifrequency synthesis using two Taylor terms (`tt0` for the spectrally flat component and `tt1` for the first order term). We convolved the `tt1` images to the common beam and stitched them together as with the `tt0` images. We then produced a complete mosaic map of α directly from the modelled Taylor terms, $\alpha = \mathtt{tt1}/\mathtt{tt0}$. Additionally, we manually computed an α map by combining the spw25+27 and spw33+35 images as

$$\alpha_{\rm manual} = \frac{\log(S_{33+35}/S_{25+27})}{\log(99.53/86.54)} \quad (4)$$

assuming each spw image is monochromatic.

To assess the reliability of these measurements, we compare the pixel-by-pixel α measurements for all pixels in which the signal-to-noise ratio of the spw25+27 image is greater than 10. Fig. 12 shows that only a small fraction of the total α measurements agree between the two methods. We have no *a priori* reason to favour one estimate over another, so we recommend that, in general, in-band spectral index measurements from ACES should be used with great caution. However, we assess the measurements in more detail before fully dismissing them.

Figs A1−A16 show zoomed-in cut-outs of individual regions. Each four-panel figure shows the low- and high-frequency 12 m images, the manually-calculated α image, and the feathered MUSTANG TENS plus ACES aggregate continuum image. Much of the extended regions with significant emission exhibit negative spectral index, sometimes very negative, with notable positive-index regions in Sgr C (Fig. A6), the 20 km s^{-1} cloud (Fig. A2), and F359 (Fig. A9), which is a foreground cloud (M. J. Reid et al. 2019). Locations dominated by H II regions, like the rim edges in the Pistol and Sickle nebula (Fig. A7) and the compact bright source in Sgr B1 (Fig. A5), have relatively flat spectral indices ($\alpha \sim 0$), as expected for optically thin free–free emission. Non-thermal filaments are expected to have negative spectral indices, but the only such features with high enough signal-to-noise to measure α are near the Pistol & Sickle (Fig. A7). A common pattern is that $\alpha \sim 0$ towards the central peaks, with $\alpha \to -4$ immediately around the peaks (e.g. as prominently seen in much of Sgr c; A6): this pattern hints that the negative indices are caused by improved flux recovery on larger angular scales at longer wavelengths. Such a pattern is unlikely to be physical in nature.

Downloaded from academic.oup.com/mnras/article/552/2/stag354/8875763 by Liverpool John Moores University user on 02 November 2026

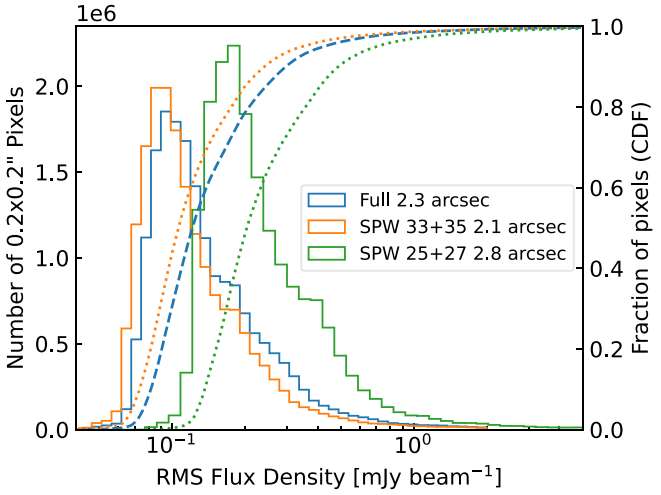


Figure 9. Histograms and cumulative distribution functions (CDFs) of the RMS maps shown in Fig. 8. For the histograms, labelled on the left axis, the X-axis is logarithmic and the *Y*-axis is linear. The CDFs are labelled on the right side and are linear. The inset legend labels the colours and provides the beam FWHM for each.

We therefore suggest that spectral indices measured towards point sources are usable if the background is adequately removed, while spectral indices towards extended regions should generally not be trusted without corroborating data.

4.2 Comparison to other data

To validate the ACES data and explore some of the consequences of the specific configurations used in ACES, we compare the ACES images to previously published ALMA observations of Sgr B2 (Section 4.2.1), the Brick (Section 4.2.2), and other CMZ clouds (Section 4.2.3). Only ALMA has observed the Galactic Centre at comparable wavelength and resolution: while CMZoom with the SMA has comparable resolution, it is at 1 mm (C. Battersby et al. 2020), and while the CARMA CMZ survey was at a similar wavelength, it has coarser resolution (M. W. Pound & F. Yusef-Zadeh 2018). In the following subsections, we compare to previously published images or those prepared by coinvestigators on ACES. A. Ginsburg et al. (2024) examined a specific continuum source in ACES and compared the ACES data to archival ALMA data; we do not repeat their analysis here, but note that that work showcases an example where it may be necessary to use data from individual ACES fields to achieve the best resolution.

4.2.1 Sgr B2

We compare the ACES image to the 2013.1.00269.S mosaic of Sgr B2, which was tied for the largest area mapped in the

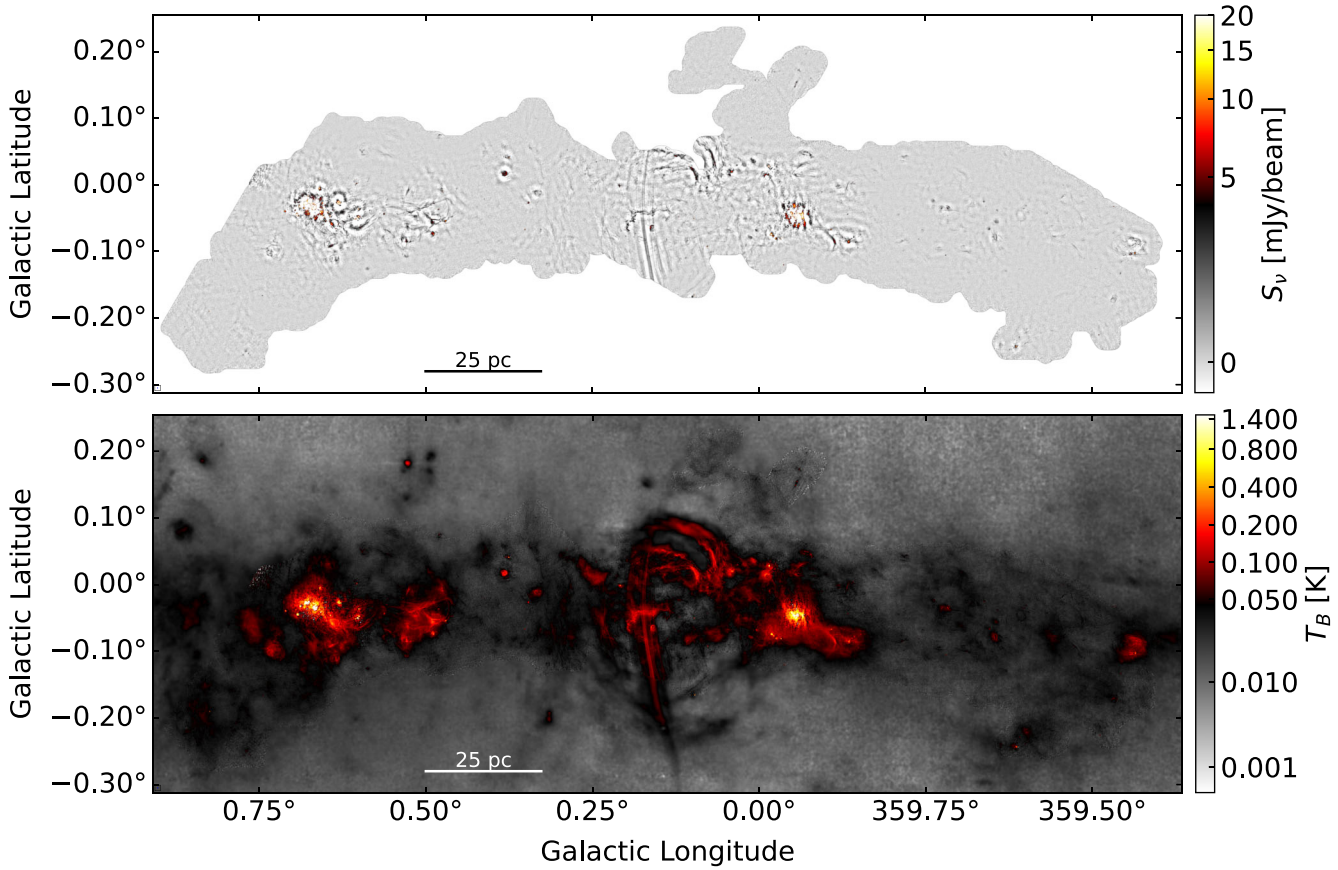


Figure 10. The full footprint mosaic ACES continuum data. The top figure shows the ACES 12 m data, the bottom figure shows the MUSTANG-2 image feathered with the ACES data. The circular beam in both figures is 2.56 arcsec and is shown in the very tiny inset box, but it is a single pixel in this figure because of print and file size limitations.

Downloaded from academic.oup.com/mnras/article/552/2/stag354/8875763 by Liverpool John Moores University user on 02 November 2026

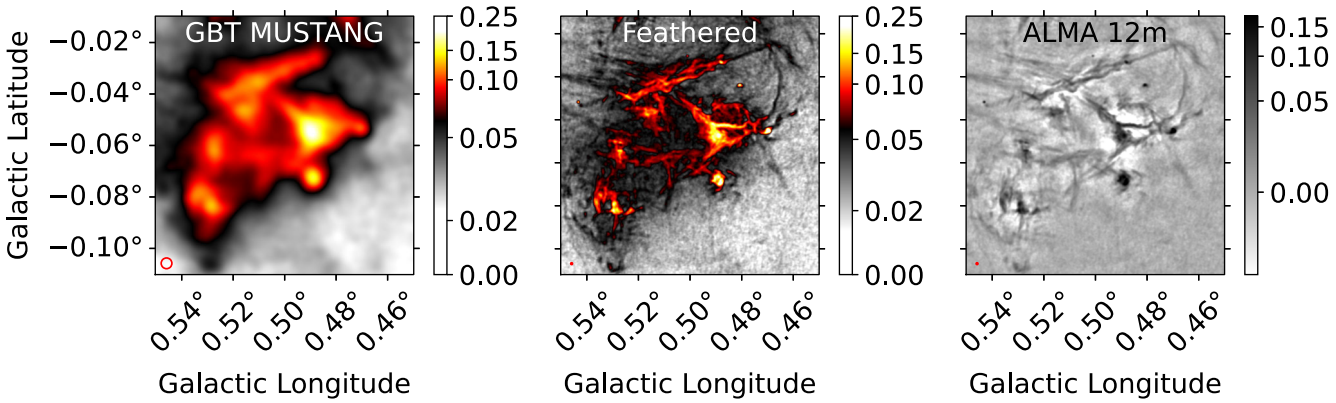


Figure 11. Comparison of the MUSTANG and ACES data and their feathered combination (see Section 3.7) in a region around Sgr B1. The units of the colourbars are in K, and the beam size (red circles) differs in the left plot from the other two. The 12 m data are intentionally shown in a different colour scale, since the missing large angular scales result in overall fainter emission and negative backgrounds.

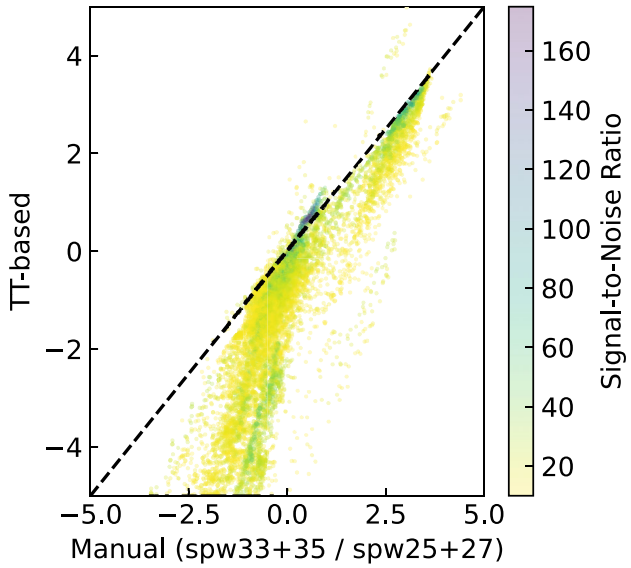


Figure 12. Spectral index α measurements from the Taylor Terms method plotted against those measured from comparison of the spw25+27 and the spw33+35 images. The points are colour-coded by signal-to-noise ratio. While there is a small tendency for higher SNR points to converge closer to the 1-1 line, there are many that are far from this line.

CMZ prior to ACES. The Sgr B2 image was presented in A. Ginsburg et al. (2018) and achieved a high dynamic range through self-calibration and the combination of data from multiple ALMA 12 m array configurations and the 7 m ACA. The image has ~ 0.5 arcsec resolution and a central effective frequency of 96.34 GHz, a little lower than the ACES aggregate image.

Fig. 14 shows a comparison between these data sets, in which the Sgr B2 image is convolved to the ACES resolution and then subtracted. In the difference image, it is apparent that the ACES data under-recover flux on scales of several to several tens of arcseconds, as expected given that the ACES images do not include 7 m ACA data and have not been self-calibrated. The difference at the peaks, Sgr B2 N, M, and S, may be caused by under-cleaning in ACES or a failure to reject line contaminants in the 2013 data set. The ACES continuum selection was not optimized for the Sgr B2 hot cores, so it may include significant absorption features that reduce the overall flux. Because of the challenge in imaging Sgr B2 in particular, we refer readers to previous, more careful measurements of these few sources (Á. Sánchez-Monge et al. 2017) for continuum analyses.

While the central cores are poorly recovered, the regions in the 'extended Sgr B2' cloud far from the N/M/S ridge are well-recovered. There are absolute differences notable in the comparison image, but they are mostly unstructured on the scales of the ACES data, indicating good recovery. Nevertheless, for this region, it is evident that the archival data outperform the ACES data in several regards.

4.2.2 G0.253+0.016: The brick

J. M. Rathborne et al. (2015) published one of the first mosaics created by ALMA, a Cycle 0 (C0) band 3 image of the Brick. Their image had an effective central frequency $\nu_{\rm obs} = 94.125$ GHz, reported noise $\sigma_{RMS} = 0.025$ mJy beam^{-1} (a few times better than ACES), and 1.7 arcsec resolution. The better sensitivity was achieved despite having fewer antennae (25 versus 40–45 in typical ACES observations) by making a smaller mosaic (13 pointings) and revisiting the field six times (compared to two visits spread over 95 pointings for ACES; see Table B1). The resulting images are evidently of higher quality, with better (u, v) coverage in addition to better sensitivity. Fig. 15 shows the comparison between the ACES and Brick data. Larger-scale emission is better recovered in the C0 data.

In order to fill in the short spacing (large angular scale) emission, J. M. Rathborne et al. (2015) extrapolated from a different wavelength. They scaled the Herschel 500 μm image using a fixed spectral index $\alpha = 3.2$. By contrast, we use the MUSTANG TENS 3 mm image, taken at nearly the same wavelength as the ACES data, to fill in our short spacing. We compare these images in Fig. 16, resulting in a striking difference: there is a north–south intensity gradient in the image, with the southern half of the Brick much brighter than the north. This difference was apparent in the original publication showing the MUSTANG-2 data (A. Ginsburg et al. 2020) but was not commented on there. The excess emission in the south implies that there is substantial

Downloaded from academic.oup.com/mnras/article/552/2/stag354/8875763 by Liverpool John Moores University user on 02 November 2026

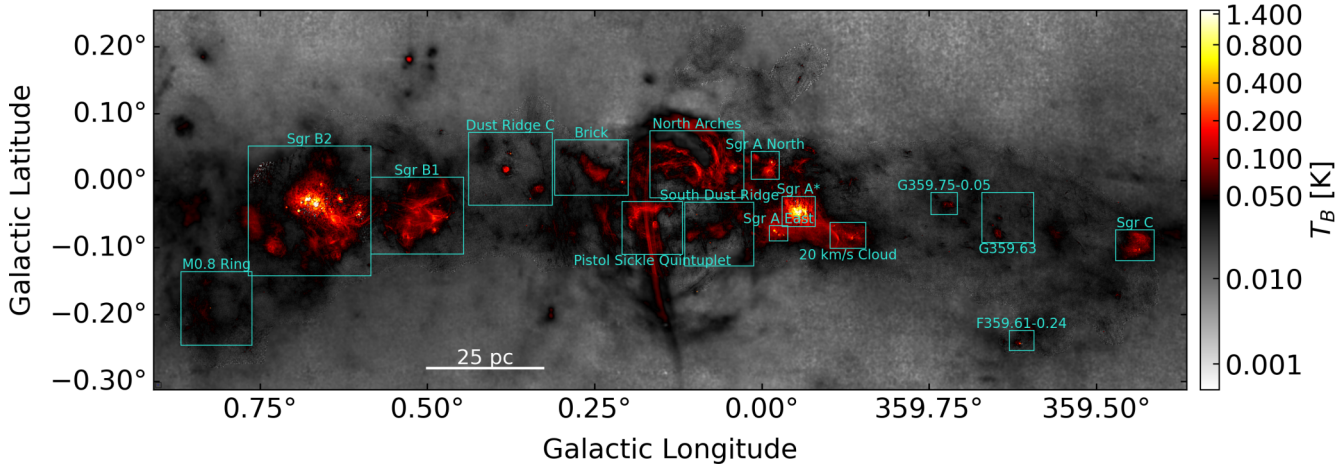


Figure 13. Repeat of Fig. 10 with added labels showing the zoom-in figure extraction locations for Figs A1–A16.

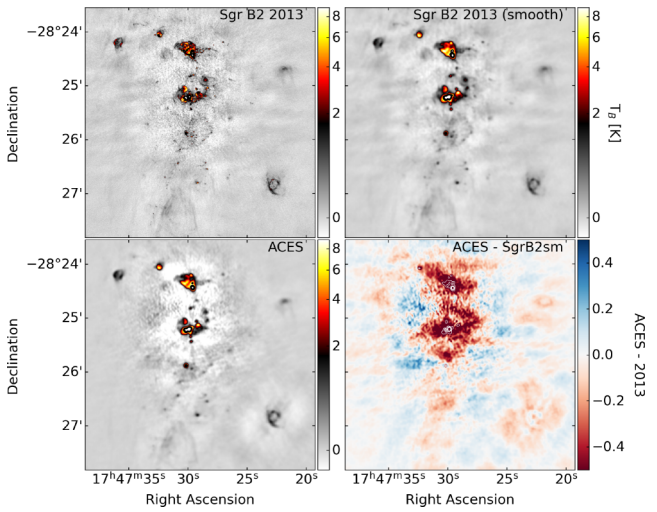


Figure 14. -bComparison between the ACES 12 m and Sgr B2 2013.1.00269.S (A. Ginsburg et al. 2018) images. (Top left) The published image from A. Ginsburg et al. (2018), (top right) the same image smoothed to ACES resolution, (bottom left) the ACES image, and (bottom right) the difference between the ACES image and the smoothed A. Ginsburg et al. (2018) image. The contours in the bottom-right panel are at [−1, −2, −3, −4, −5] K.

free-free contribution to the 3 mm emission in the Brick that is not accounted for in the Herschel extrapolation.

To evaluate the nature of the disagreement further, we compare to the MEERKAT 1.4 GHz (I. Heywood et al. 2022) image in Fig. 17. To attempt to match the MEERKAT and ACES data, we scaled the MEERKAT to 95 GHz adopting $\alpha = -0.1$, as expected for optically thin free–free emission. Fig. 17 shows that subtracting the scaled MEERKAT image from the ACES+TENS image brings the latter into closer agreement with the J. M. Rathborne et al. (2015) image, but there still remains some variation, either because the spectral index spatially varies or because of a genuine excess at 3 mm in the southern portion of the Brick.

Understanding the spatial and spectral structure of the Brick specifically (J. M. Rathborne et al. 2015; C. Federrath et al. 2016; J. D. Henshaw et al. 2019; D. L. Walker et al. 2021; A. Ginsburg et al. 2023; M. A. Petkova et al. 2023; Y. Sofue 2024), and any gas structure in the CMZ more generally, clearly remains an open challenge. We defer further analysis to future work.

4.2.3 Other CMZ dense clouds

As part of program 2018.1.01420.S (PI: Xing Lu), F. Xu et al. (2025) surveyed the Sgr C, Cloud E, and 20 km s^{-1} clouds using ALMA in configuration C-4 and C-7. We compare to the shorter-baseline C-4 images in Figs 18 and 19. In the 20 km s^{-1} cloud and Cloud E, there is small disagreement on large angular scales, which we attribute to the difference in (u, v) coverage between the ACES and Xu data sets. In Sgr C, there is some disagreement in the small-scale structures at the few percent level; this difference is also attributable to differences in (u, v) coverage, but may be slightly amplified by the small difference in frequency coverage of ACES versus F. Xu et al.

While these targeted observations provide higher resolution, more detailed views of the star-forming clumps and cores, the ACES mosaics provide a view of the large-scale context.

5 SUMMARY

We have presented the continuum data from the ALMA ACES Large Program supplemented by the GBT TENS MUSTANG project.

These data include:

(i) A $\sim$ 3 mm image produced using only 12 m array data with $\approx$ 0.1 mJy beam^{-1} sensitivity and 2.4 arcsec beam. The largest angular scale recovered in these images is roughly 10–20 arcsec.

(ii) Two monochromatic images at 86.5 and 99.5 GHz produced from the upper- and lower- sidebands of the ALMA data, with 2.9 and 2.2 arcsec resolution and 0.2 and 0.1 mJy beam^{-1} RMS, respectively.

(iii) A feathered image combining the ACES aggregate continuum data with the MUSTANG-2 TENS image and Planck all-sky

Downloaded from academic.oup.com/mnras/article/552/2/stag354/8875763 by Liverpool John Moores University user on 02 November 2026

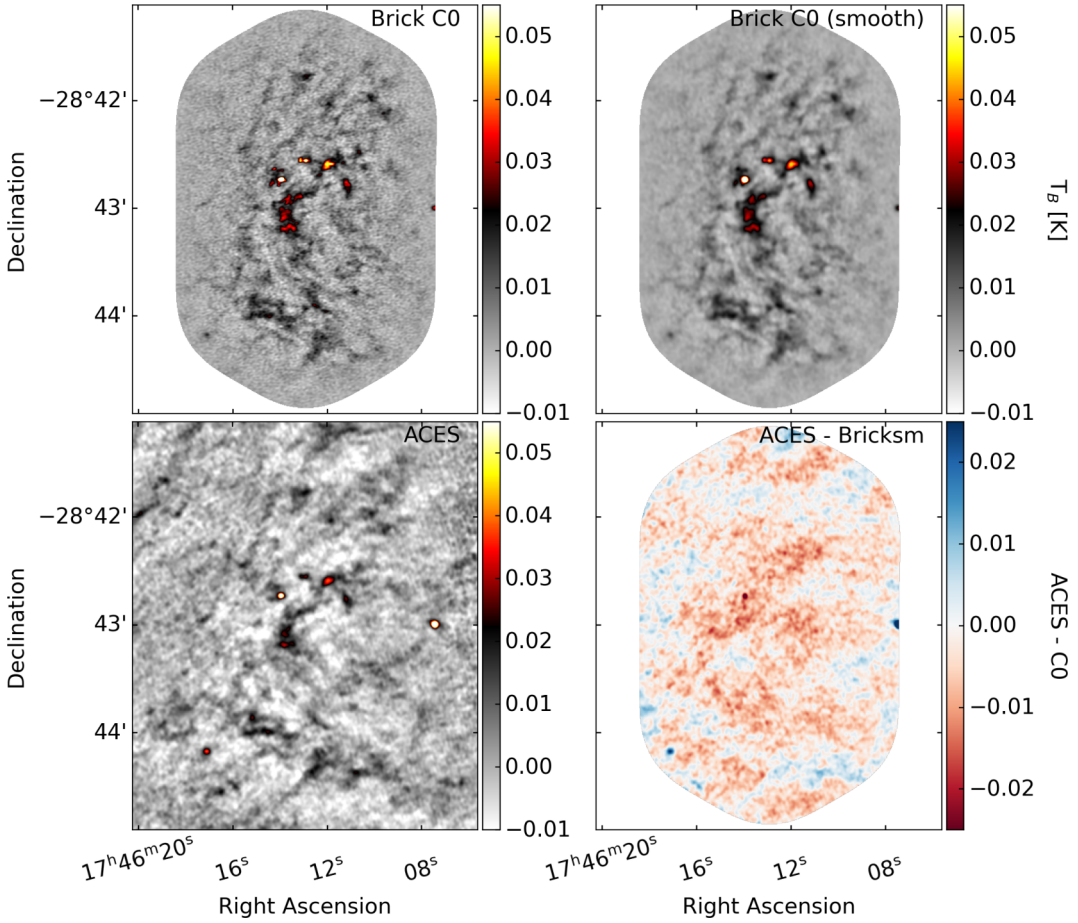


Figure 15. Comparison between ACES 12 m and the Cycle 0 mosaic of the Brick (J. M. Rathborne et al. 2015). The Brick image is not primary-beam corrected, so the signal is artificially suppressed around the edges of the C0 image.

data. This image is sensitive to all angular scales, but is comprised of individual images with different spatial frequency sensitivity.

(iv) Images of the in-band spectral index, measured both using CASA's MTMFS imaging and by taking the ratio of the low- and high-frequency ACES mosaic images.

Appendix A shows zoom-in views of some of the most prominent features in the CMZ, highlighting the regions where spectral index measurements are most significantly detected.

We performed basic quality assessment analyses by comparing the ACES data to previous ALMA observations. We found overall good agreement with a few exceptions:

(i) Imaging programs with better (u, v) coverage outperform ACES.

(ii) Towards bright sources (Sgr B2 and Sgr A$*$), programs that have undergone careful self-calibration and/or time-dependent calibration outperform ACES.

Otherwise, for most of the CMZ, ACES represents the new standard for millimeter continuum observations.

ACKNOWLEDGEMENTS

The paper was instigated and led by the ACES data reduction working group, which is coordinated by Adam Ginsburg, Daniel Walker, and Ashley Barnes, and includes (alphabetically) Nazar Budaiev, Laura Colzi, Claire Cooke, Savannah Gramze, Pei-Ying Hsieh, Katharina Immer, Desmond Jeff, Xing Lu, Elisabeth Mills, Jaime Pineda, Marc Pound, Álvaro Sánchez-Monge, and Qizhou Zhang. ACES is led by Principal Investigator Steven Longmore, together with co-PIs and the management team, John Bally, Ashley Barnes, Cara Battersby, Laura Colzi, Adam Ginsburg, Jonathan Henshaw, Paul Ho, Izaskun Jiménez-Serra, Elisabeth Mills, Maya Petkova, Mattia Sormani, Robin Tress, Daniel Walker, and Jennifer Wallace. The ACES proposal was led by Principal Investigator Steven Longmore, together with co-PIs John Bally, Cara Battersby, Adam Ginsburg, Jonathan Henshaw, Paul Ho, J. M. Diederik Kruijssen, Izaskun Jiménez-Serra, and Elisabeth Mills. The remaining coauthors comprise the ACES team, and its members contributed to the proposal, data analysis, idea development, and/or reading and commenting on the manuscript.

AG acknowledges support from the NSF under grants CAREER 2142300, AAG 2008101, and particularly AAG 2206511 that supports the ACES large program. IJ-S, LC, and VMR acknowledge support from the grant PID2022-136814NB-I00 by the Spanish Ministry of Science, Innovation and Universities/State Agency of Research MICIU/AEI/10.13039/501100011033 and by ERDF, UE. IJ-S also acknowledges the ERC Consolidator grant OPENS (project number 101125858) funded by the European Union. VMR also acknowledges the grant RYC2020-029387-I funded by MICIU/AEI/10.13039/501100011033 and by 'ESF, Investing in your future', and from the Consejo Superior de Investigaciones Científicas (CSIC) and the Centro de

Downloaded from academic.oup.com/mnras/article/552/2/stag354/8875763 by Liverpool John Moores University user on 02 November 2026

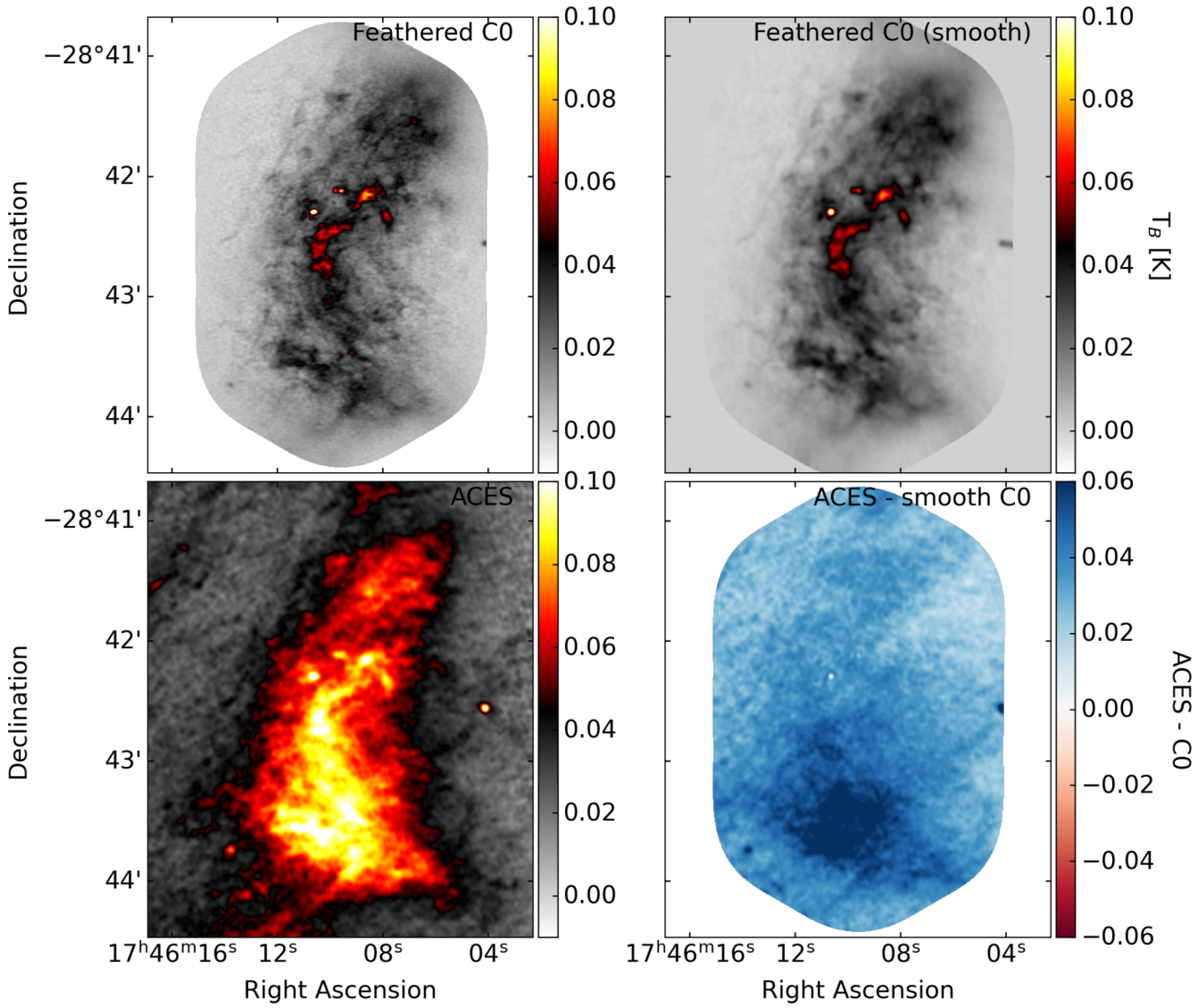


Figure 16. Comparison between ACES plus TENS image and the Cycle 0 mosaic of the Brick that included short-spacing (J. M. Rathborne et al. 2015). The bottom left panel shows the ACES minus scaled MEERKAT minus the Cycle 0 combined with rescaled Herschel image. This is intended to show the difference between the ACES+MUSTANG-2 combination and the ALMA Cycle 0 + extrapolated Herschel data after accounting for any free-free contamination in the ACES and MUSTANG-2 data.

Astrobiología (CAB) through the project 20225AT015 (Proyectos intramurales especiales del CSIC); and from the grant CNS2023-144464 funded by MICIU/AEI/10.13039/501100011033 and by "European Union NextGenerationEU/PRTR. CF acknowledges funding provided by the Australian Research Council (Discovery Project grants DP230102280 and DP250101526), and the Australia-Germany Joint Research Cooperation Scheme (UA-DAAD). The authors acknowledge UFIT Research Computing for providing computational resources and support that have contributed to the research results reported in this publication. RF acknowledges support from the grants PID2023-146295NB-I00, and from the Severo Ochoa grant CEX2021-001131-S funded by MCIN/AEI/ 10.13039/501100011033 and by 'European Union NextGenerationEU/PRTR'. DLW gratefully acknowledges support from the UK ALMA Regional Centre (ARC) Node, which is supported by the Science and Technology Facilities Council [grant numbers ST/Y004108/1 and ST/T001488/1]. COOL Research DAO (M. Chevance, J. M. D. Kruijssen & S. N. Longmore 2025) is a Decentralized Autonomous Organization supporting research in astrophysics aimed at uncovering our cosmic origins. C.B. gratefully acknowledges funding from National Science Foundation under Award Nos. 2108938, 2206510, and CAREER 2145689, as well as from the National Aeronautics and Space Administration through the Astrophysics Data Analysis Program under Award '3-D MC: Mapping Circumnuclear Molecular Clouds from X-ray to Radio,' Grant No. 80NSSC22K1125. This paper makes use of the following ALMA data: ADS/JAO.ALMA#2021.1.00172.L, ADS/JAO.ALMA#2013.1.00269.S, ADS/JAO.ALMA#2011.0.00217.S. ALMA is a partnership of ESO (representing its member states), NSF (USA) and NINS (Japan), together with NRC (Canada), NSTC and ASIAA (Taiwan), and KASI (Republic of Korea),

Downloaded from academic.oup.com/mnras/article/552/2/stag354/8875763 by Liverpool John Moores University user on 02 November 2026

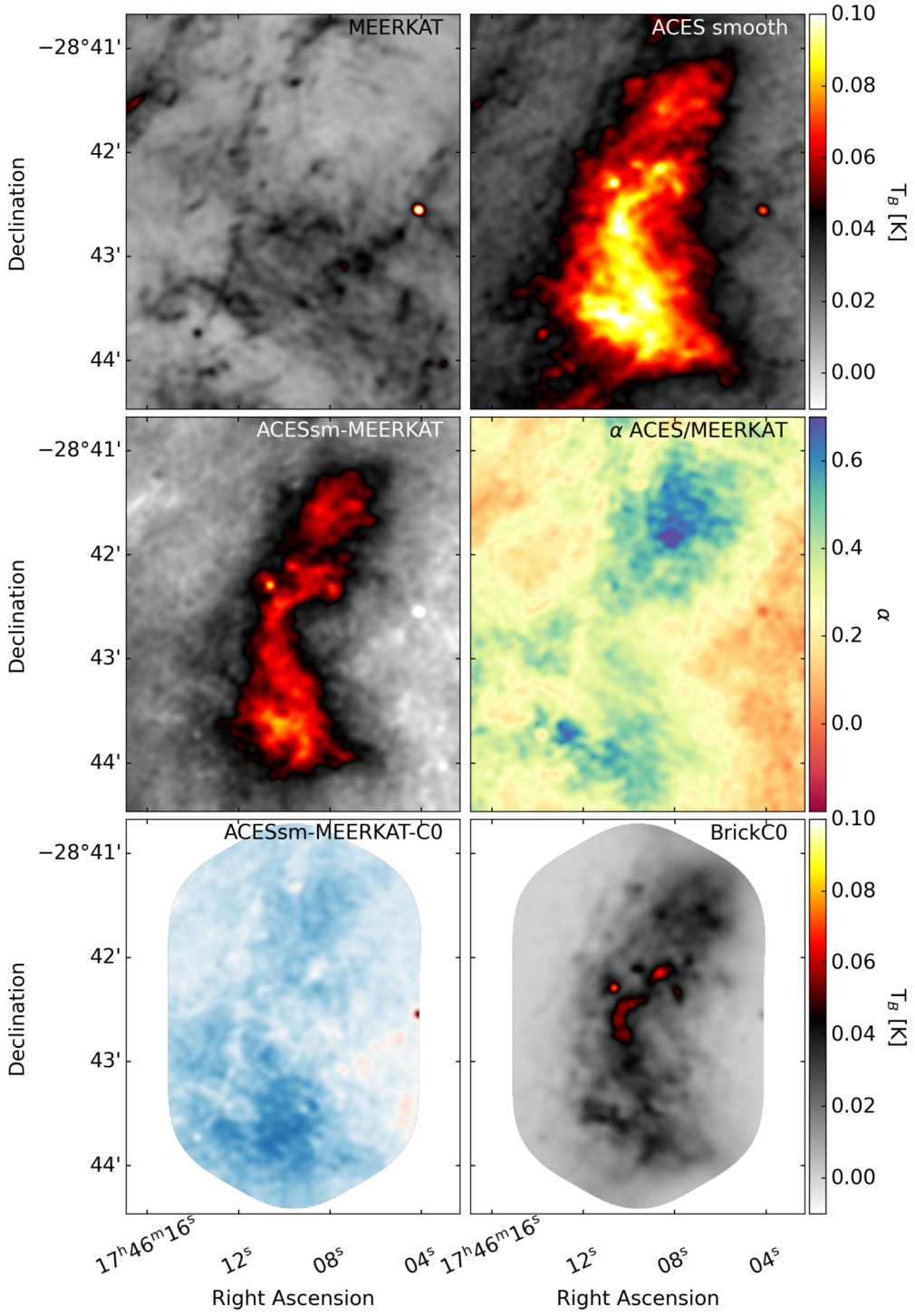


Figure 17. Comparison between ACES plus TENS image and the MEERKAT 1.4 GHz image from I. Heywood et al. (2022).The MEERKAT image has been scaled by $\alpha = -0.1$ and is shown in brightness temperature units at $\nu = 97.1$ GHz such that the colourbars are identical. The bottom-left panel shows the same image as the bottom-right panel of Fig. 16 after subtracting the scaled MEERKAT image.

in cooperation with the Republic of Chile. The Joint ALMA Observatory is operated by ESO, AUI/NRAO, and NAOJ. The authors are grateful to the staff throughout the ALMA organisation, particularly those at the European ALMA Regional Centre, the Joint ALMA Observatory, and the UK ALMA Regional Centre Node, for their extensive support, which was essential to the success of this challenging Large Program. The GBT data were acquired under projects GBT23A-268 & GBT18A-014. The National Radio Astronomy Observatory and Green Bank Observatory are facilities of the U.S. National Science Foundation operated under cooperative agreement by Associated Universities, Inc. FHL acknowledges support from the ESO Studentship Programme, the Scatcherd European Scholarship of the University of Oxford, and the European

Downloaded from academic.oup.com/mnras/article/552/2/stag354/8875763 by Liverpool John Moores University user on 02 November 2026

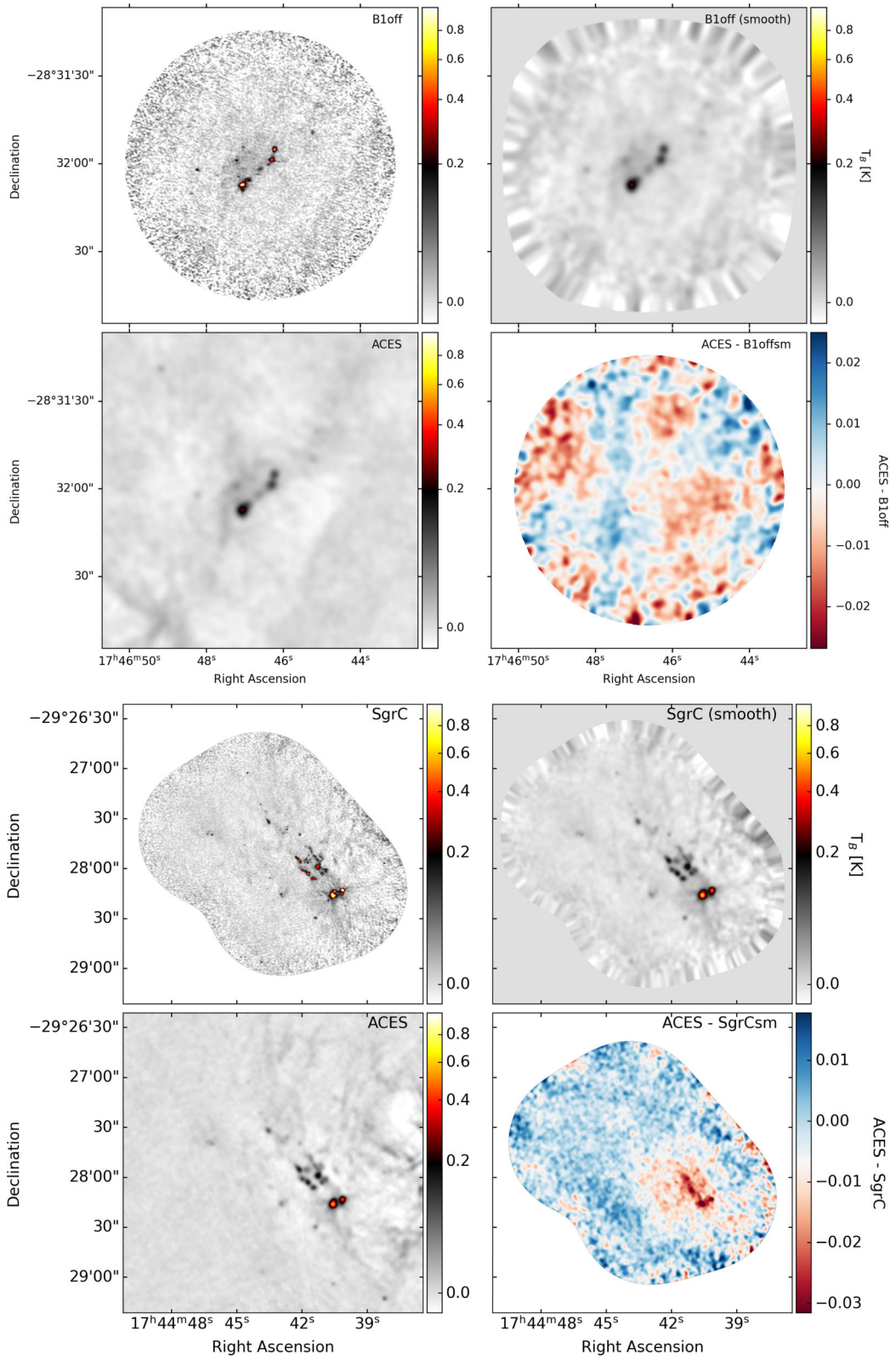


Figure 18. Comparison of ACES to F. Xu et al. (2025) observations of the G0.6 cloud region and Sgr C.

Research Council's starting grant ERC StG-101077573 ('ISM-METALS'). J.Wallace gratefully acknowledges funding from National Science Foundation under Award Nos. 2108938 and 2206510. EAC Mills gratefully acknowledges funding from the National Science Foundation under Award Nos. 1813765, 2115428, 2206509, and CAREER 2339670. FN-L gratefully acknowledges financial support from grant PID2024-162148NA-I00, funded by MCIN/AEI/10.13039/501100011033 and the

Downloaded from academic.oup.com/mnras/article/552/2/stag354/8875763 by Liverpool John Moores University user on 02 November 2026

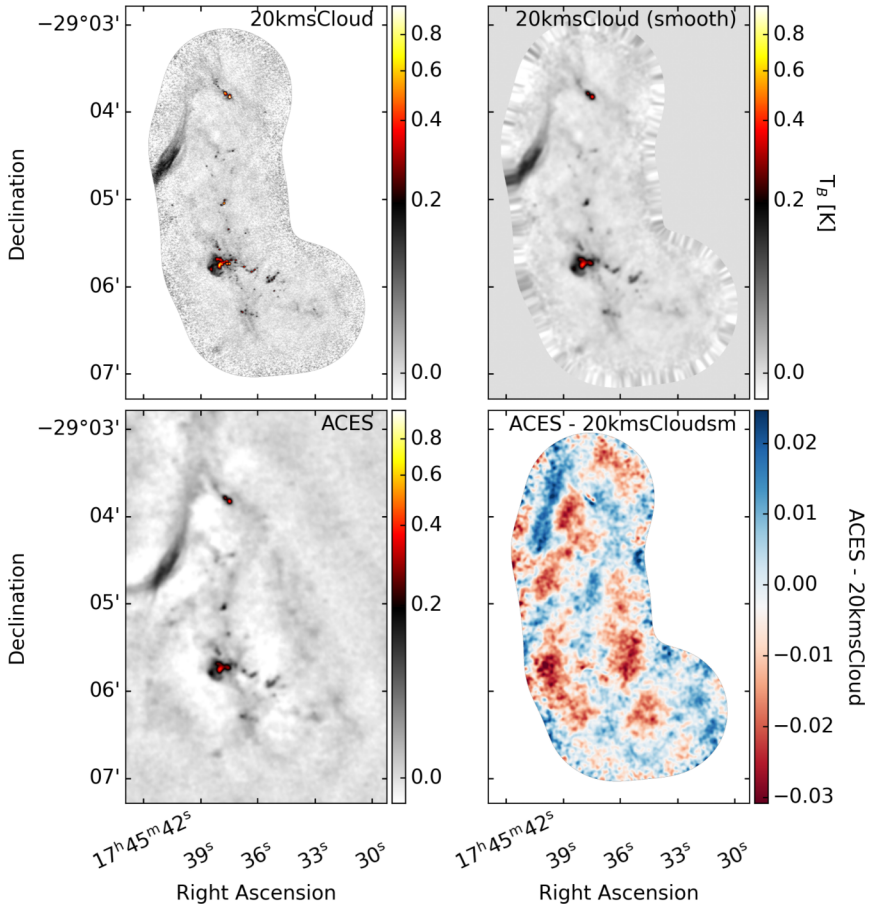


Figure 19. Comparison of ACES to F. Xu et al. (2025) observations of the 20 km s^{-1} cloud.

European Regional Development Fund (ERDF) 'A way of making Europe', from the Ramón y Cajal programme (RYC2023-044924-I) funded by MCIN/AEI/10.13039/501100011033 and FSE+, and from the Severo Ochoa grant CEX2021-001131-S, funded by MCIN/AEI/10.13039/501100011033. K.M.D. acknowledges support from the European Research Council (ERC) Advanced Grant MOPPEX 833460.The project that gave rise to these results received the support of a fellowship from the "la Caixa" Foundation (ID 100010434)". The fellowship code is LCF/BQ/PR25/12110012.

DATA AVAILABILITY

All data products and associated documentation can be found at https://almascience.org/alma-data/lp/aces.

All code and data processing issues are available at the public GitHub repository here: https://github.com/ACES-CMZ/reduction_ACES.

The ACES pipeline is based on a number of open-source astronomy software packages, including ASTROPY (Astropy Collaboration 2013, 2018, 2022), ASTROQUERY (A. Ginsburg et al. 2019b), SPECTRAL-CUBE (A. Ginsburg et al. 2019a), RADIO-BEAM (E. Koch et al. 2025), pvextractor (A. Ginsburg, T. Robitaille & C. Beaumont 2016), REPROJECT (T. Robitaille, C. Deil & A. Ginsburg 2020), IMAGE_REGISTRATION (A. Ginsburg & A. Giessel 2014), STATCONT (Á. Sánchez-Monge et al. 2018), CASA (CASA Team et al. 2022), NUMPY (C. R. Harris et al. 2020), CARTA (A. Comrie et al. 2021), and MATPLOTLIB (J. D. Hunter 2007).

REFERENCES

Aguirre J. E. et al., 2011, ApJS, 192, 4
Astropy Collaboration, 2013, A&A, 558, A33
Astropy Collaboration, 2018, AJ, 156, 123
Astropy Collaboration, 2022, ApJ, 935, 167
Bally J. et al., 2010, ApJ, 721, 137
Bally J. et al., 2025, ApJ, 983, 20
Barnes A. T., Longmore S. N., Battersby C., Bally J., Kruijssen J. M. D., Henshaw J. D., Walker D. L., 2017, MNRAS, 469, 2263
Battersby C. et al., 2020, ApJS, 249, 35
Bulatek A., Ginsburg A., Darling J., Henkel C., Menten K. M., 2023, ApJ, 956, 78
CASA Team et al., 2022, PASP, 134, 114501
Chevance M., Kruijssen J. M. D., Longmore S. N., 2025, preprint (arXiv:2501.13160)
Comrie A. et al., 2021, CARTA: The Cube Analysis and Rendering Tool for Astronomy. Zenodo, https://ui.adsabs.harvard.edu/abs/2021zndo...3377984C/abstract
Cornwell T. J., 1988, A&A, 202, 316
Cotton W. D., 2017, PASP, 129, 094501
Dicker S. R. et al., 2014, J. Low Temp. Phys., 176, 808
Ekers R. D., Rots A. H., 1979, in van Schooneveld C., ed., Astrophysics and Space Science Library Vol. 76, IAU Colloq. 49: Image Formation from Coherence Functions in Astronomy. C. D. Reidel Publishing Co., p. 61, preprint (arXiv:1212.3311)
Event Horizon Telescope Collaboration et al., 2022, ApJ, 930, L12
Federrath C. et al., 2016, ApJ, 832, 143
Genzel R., Eisenhauer F., Gillessen S., 2010, Rev. Mod. Phys., 82, 3121
Ginsburg A., Giessel A., 2014, image_registration v0.2.1. Zenodo, https://ui.adsabs.harvard.edu/abs/2014zndo.....12528G/abstract
Ginsburg A. et al., 2013, ApJS, 208, 14

Downloaded from academic.oup.com/mnras/article/552/2/stag354/8875763 by Liverpool John Moores University user on 02 November 2026

Ginsburg A., Robitaille T., Beaumont C., 2016, Astrophysics Source Code Library, record ascl:1608.010
Ginsburg A. et al., 2018, ApJ, 853, 171
Ginsburg A. et al., 2019a, radio-astro-tools/spectral-cube: Release v0.4.5. Zenodo, https://ui.adsabs.harvard.edu/abs/2019zndo...2573901G/abstract
Ginsburg A. et al., 2019b, AJ, 157, 98
Ginsburg A. et al., 2020, ApJS, 248, 24
Ginsburg A. et al., 2022, A&A, 662, A9
Ginsburg A. et al., 2023, ApJ, 959, 36
Ginsburg A. et al., 2024, ApJ, 968, L11
Harris C. R. et al., 2020, Nature, 585, 357
Heard V., Warwick R. S., 2013, MNRAS, 428, 3462
Henshaw J. D. et al., 2019, MNRAS, 485, 2457
Henshaw J. D., Barnes A. T., Battersby C., Ginsburg A., Sormani M. C., Walker D. L., 2023, in Inutsuka S., Aikawa Y., Muto T., Tomida K., Tamura M., eds, Proc. ASP Conf. Ser. Vol. 534,, Protostars and Planets VII. Astron. Soc. Pac., San Francisco, p. 83
Heywood I. et al., 2022, ApJ, 925, 165
Hsieh P.-Y., ACES Team, 2025, MNRAS, xxx, yyy
Hunter J. D., 2007, Comput. Sci. Eng., 9, 90
Koch E. et al., 2025, radio-astro-tools/radio-beam: v0.3.9. Zenodo, https://ui.adsabs.harvard.edu/abs/2025zndo..15677957K/abstract
Kruijssen J. M. D., Longmore S. N., Elmegreen B. G., Murray N., Bally J., Testi L., Kennicutt R. C., 2014, MNRAS, 440, 3370
Krumholz M. R., Kruijssen J. M. D., Crocker R. M., 2017, MNRAS, 466, 1213
Kunneriath D. et al., 2012, A&A, 538, A127
Law C. J., Yusef-Zadeh F., Cotton W. D., Maddalena R. J., 2008a, ApJS, 177, 255
Law C. J., Yusef-Zadeh F., Cotton W. D., 2008b, ApJS, 177, 515
Leroy A. K. et al., 2021, ApJS, 255, 19
Longmore S. N., ACES Team, 2025, MNRAS, xxx, yyy
Longmore S. N. et al., 2013, MNRAS, 429, 987
Lu X., ACES Team, 2025, MNRAS, xxx, yyy
Molinari S. et al., 2011, ApJ, 735, L33
Muno M. P. et al., 2009, ApJS, 181, 110
Nogueras-Lara F. et al., 2018, A&A, 610, A83
Nonhebel M. et al., 2024, A&A, 691, A70
Petkova M. A. et al., 2023, MNRAS, 520, 2245
Pety J., Rodríguez-Fernández N., 2010, A&A, 517, A12
Planck Collaboration I, 2014, A&A, 571, A1
Pound M. W., Yusef-Zadeh F., 2018, MNRAS, 473, 2899
Rathborne J. M. et al., 2015, ApJ, 802, 125
Rau U., Naik N., Braun T., 2019, AJ, 158, 3
Reid M. J. et al., 2019, ApJ, 885, 131
Robitaille T., Deil C., Ginsburg A., 2020, Astrophysics Source Code Library, ascl:2011.023
Sánchez-Monge Á. et al., 2017, A&A, 604, A6
Sánchez-Monge Á., Schilke P., Ginsburg A., Cesaroni R., Schmiedeke A., 2018, A&A, 609, A101
Sofue Y., 2024, PASJ, 76, 773
Sormani M. C. et al., 2020, MNRAS, 497, 5024
Tang Y., Wang Q. D., Wilson G. W., 2021a, MNRAS, 505, 2377
Tang Y. et al., 2021b, MNRAS, 505, 2392
Veilleux S., Cecil G., Bland-Hawthorn J., 2005, ARA&A, 43, 769
Walker D., ACES Team, 2025, MNRAS, xxx, yyy
Walker D. L. et al., 2021, MNRAS, 503, 77
Wang Q. D., Gotthelf E. V., Lang C. C., 2002, Nature, 415, 148
Wang Q. D. et al., 2010, MNRAS, 402, 895
Xu F. et al., 2025, A&A, 697, A164

APPENDIX A: CONTINUUM ZOOM-INS

We show a series of zoom figures cut out from the regions shown in Fig. 13 in this Appendix in Figs A1–A16. These regions highlight most of the high signal-to-noise extended emission regions with significant measurements of the spectral index (see Section 4.1). The spectral index measurement used in these figures is the 'manual' index from dividing the high-frequency (spw33+35) by the low-frequency (spw25+27) ACES images. A brief analysis of each figure is given in its caption.

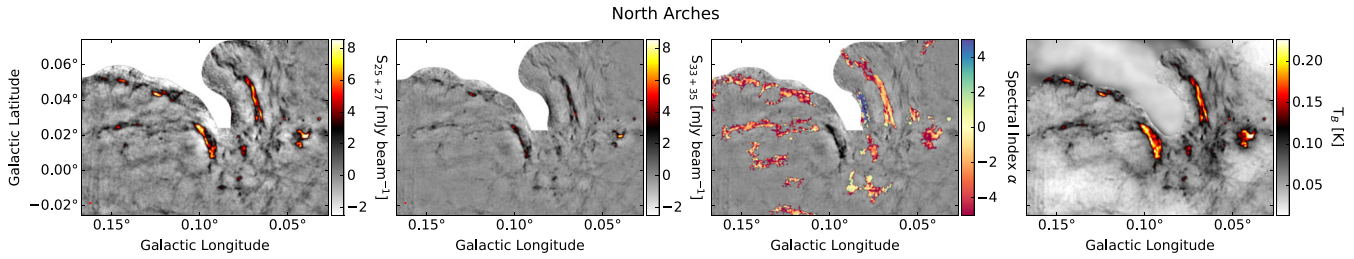


Figure A1. Cut-out image from the full mosaic showing the spw25+27 image (left), spw33+35 (centre-left), spectral index α (centre-right), and the feathered aggregate continuum plus MUSTANG (right). This cutout shows the northern Arched Filaments. These are H II regions dominated by free–free emission, but their spectral indices appear to be predominantly highly negative.

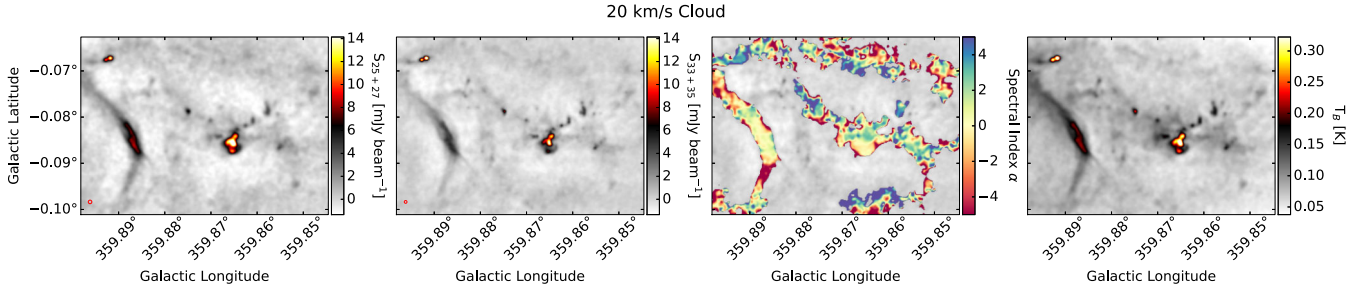


Figure A2. Like Fig. A1, but for the 20 km s^{-1} cloud. High spectral index ($\alpha \sim$ 3-4), dust-dominated regions are associated with compact, clumpy emission, while flatter indexes are associated with the filament on the left, suggesting that it is dominated by emission from hot plasma.

Downloaded from academic.oup.com/mnras/article/552/2/stag354/8875763 by Liverpool John Moores University user on 02 November 2026

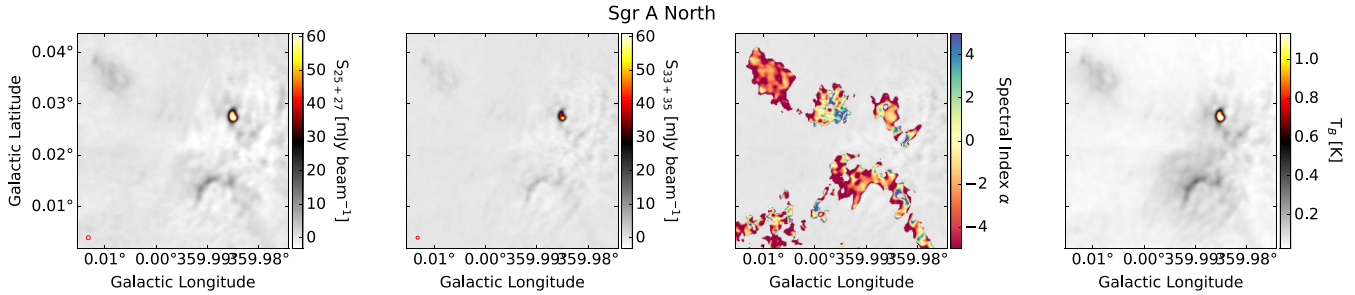


Figure A3. Like Fig. A1, but for the region north of Sgr A∗ (see Fig. 13). Most of the emission is flat or negative spectral index, indicating that there is little dust in this region.

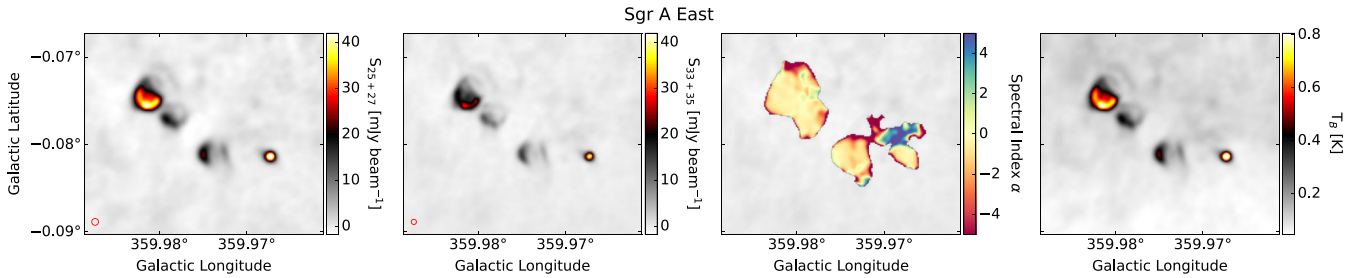


Figure A4. Like Fig. A1, but for Sgr A East (see Fig. 13). The circular objects are known H II regions, and they correspondingly exhibit flat spectral indices, though there is also a faint ridge of high-index (dust-dominated) emission connecting the rightmost two.

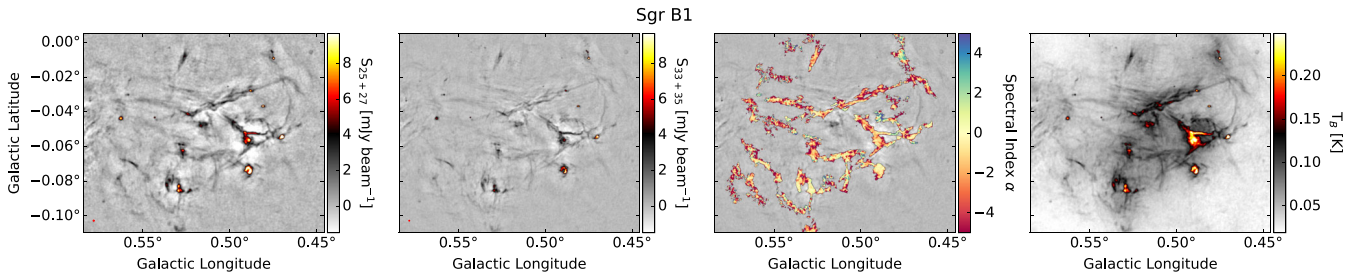


Figure A5. Like Fig. A1, but for Sgr B1 (see Fig. 13). The Sgr B1 region is comprised primarily of extended H II regions, and the spectral index is correspondingly flat or negative.

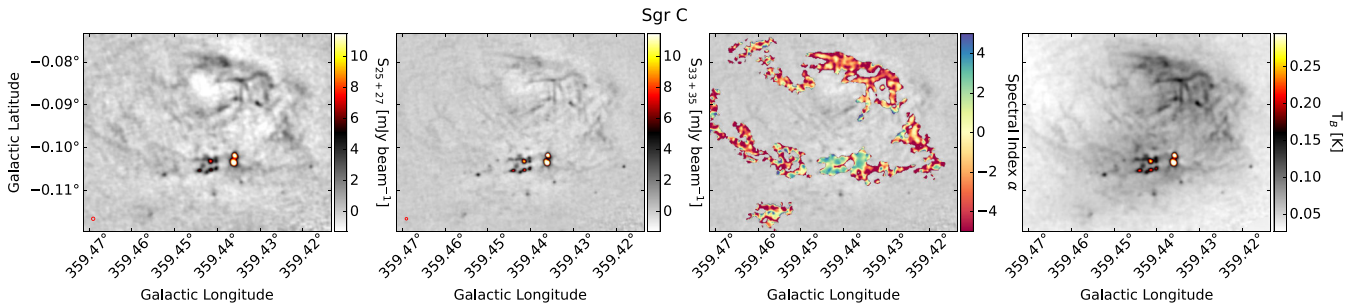


Figure A6. Like Fig. A1, but for Sgr C (see Fig. 13). The dust cores in the bottom centre are clearly steep index ($\alpha \sim$ 3-4) and dust-dominated, while the remainder of the extended emission is produced by plasma emission (J. Bally et al. 2024).

Downloaded from academic.oup.com/mnras/article/552/2/stag354/8875763 by Liverpool John Moores University user on 02 November 2026

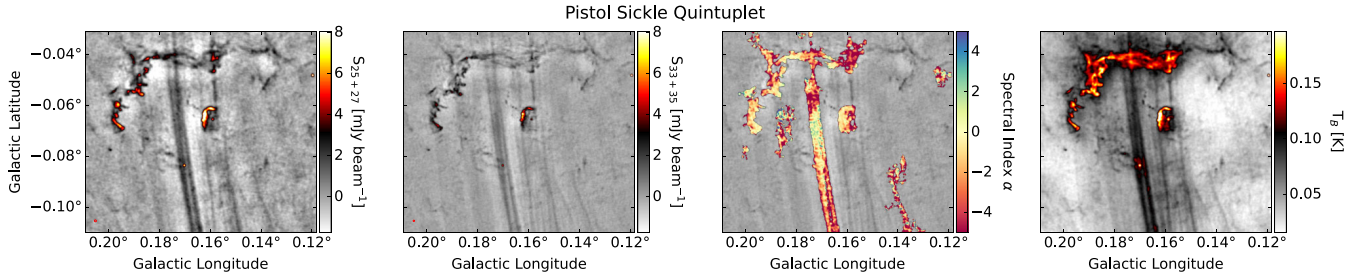


Figure A7. Like Fig. A1, but for the Pistol, Sickle, and Quintuplet region (see Fig. 13). The large-scale arced feature is the Sickle HII region, while the vertical streaked features are part of the non-thermal arch filaments. The emission in this region is mostly flat or negative ($\alpha < 2$), consistent with plasma emission.

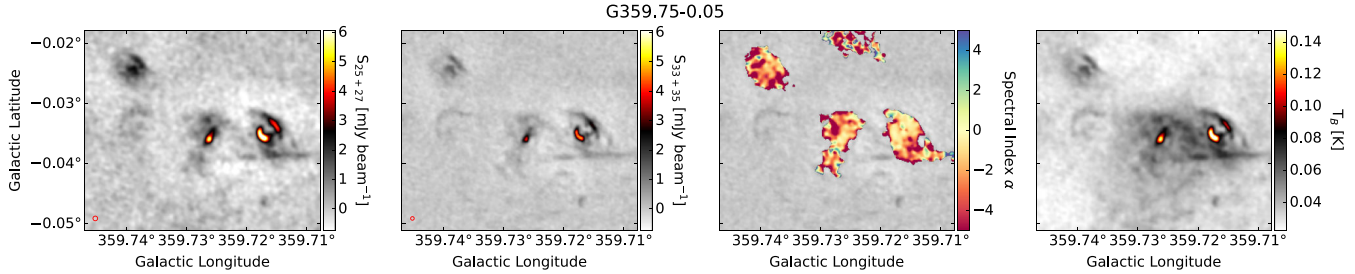


Figure A8. Like Fig. A1, but for the G359.75-0.05 region (see Fig. 13). Because of the flat spectral indices ($\alpha \lesssim 0$), this region appears to be dominated by plasma emission.

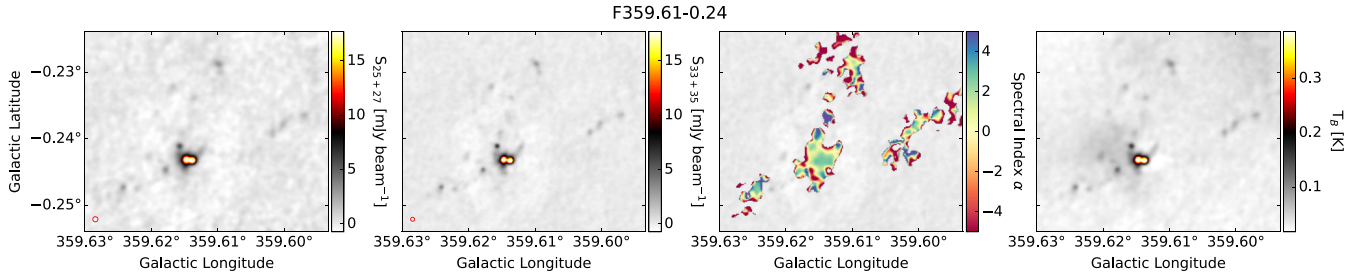


Figure A9. Like Fig. A1, but for the G359.61-0.24 region (see Fig. 13). This region is a known foreground cloud (M. J. Reid et al. 2019) and is dust-dominated based on its spectral indexes.

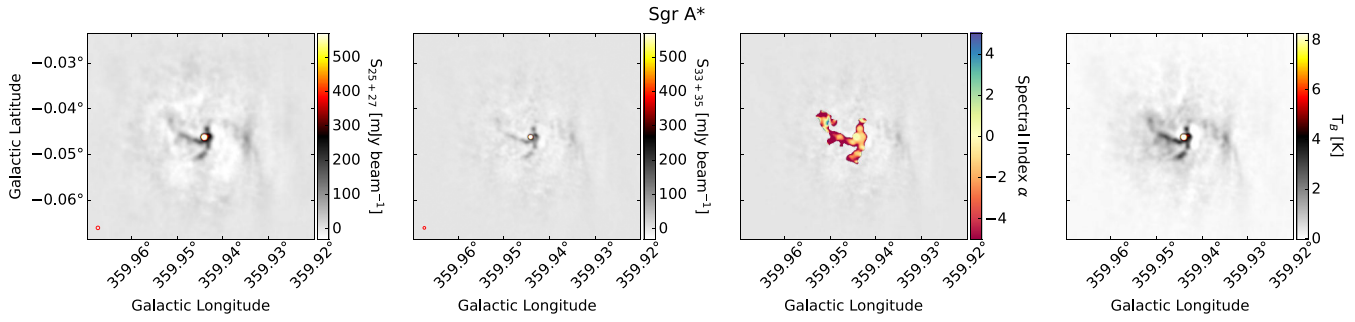


Figure A10. Like Fig. A1, but for Sgr A∗ (see Fig. 13). The negative spectral index observed in the minispiral is consistent with previous measurements (D. Kunneriath et al. 2012).

Downloaded from academic.oup.com/mnras/article/552/2/stag354/8875763 by Liverpool John Moores University user on 02 November 2026

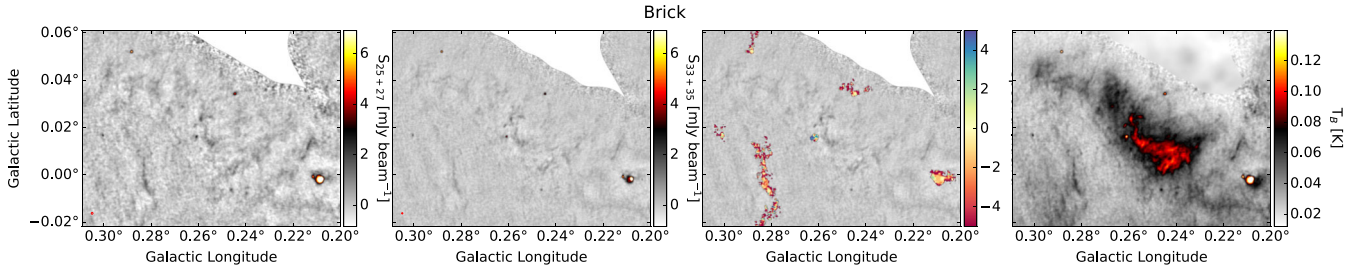


Figure A11. Like Fig. A1, but for The Brick (see Fig. 13). As noted in Section 4.2.2, the Brick is mostly resolved out in ACES images, so there is no measurement of the spectral index within the main body of the cloud. Only the known small star-cluster-forming region (D. L. Walker et al. 2021; A. Bulatek et al. 2023) has a dustlike index.

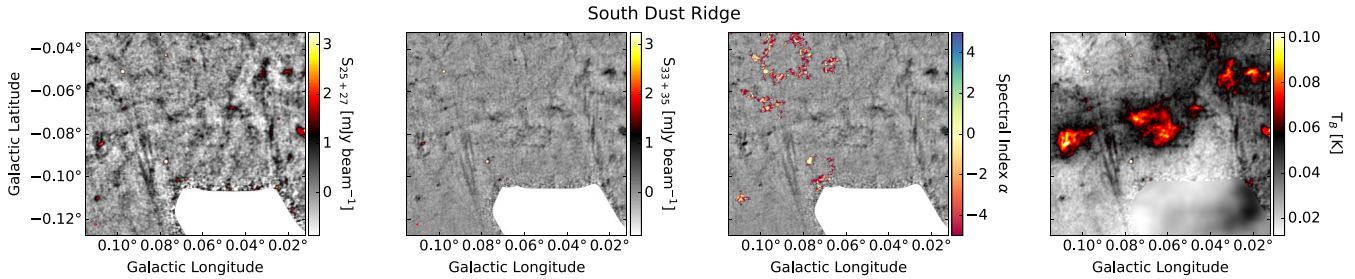


Figure A12. Like Fig. A1, but for the southern dust ridge region, also know as the 'Three Little Pigs' (see Fig. 13 C. Battersby et al. 2020). Like The Brick (Fig. A11), most of the cloud emission is resolved out. The extended emission with detected spectral index is most likely plasma.

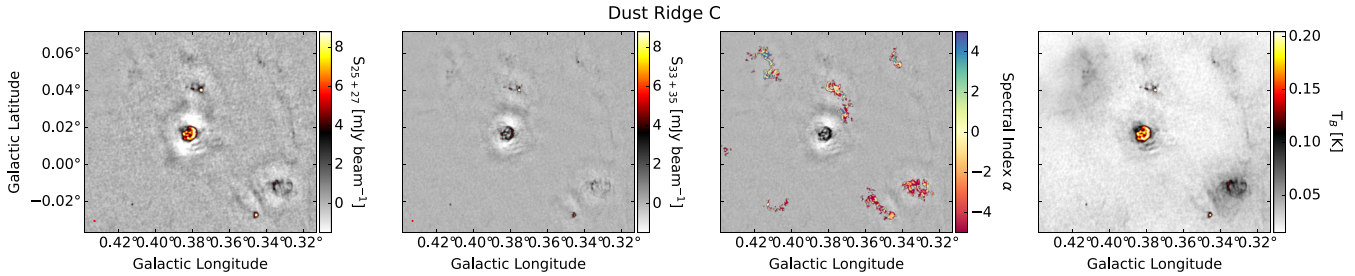


Figure A13. Like Fig. A1, but for Dust Ridge Cloud C (see Fig. 13). Because of the deep negative bowls around the central HII region in this image, it did not pass the signal-to-noise threshold used to make the α maps.

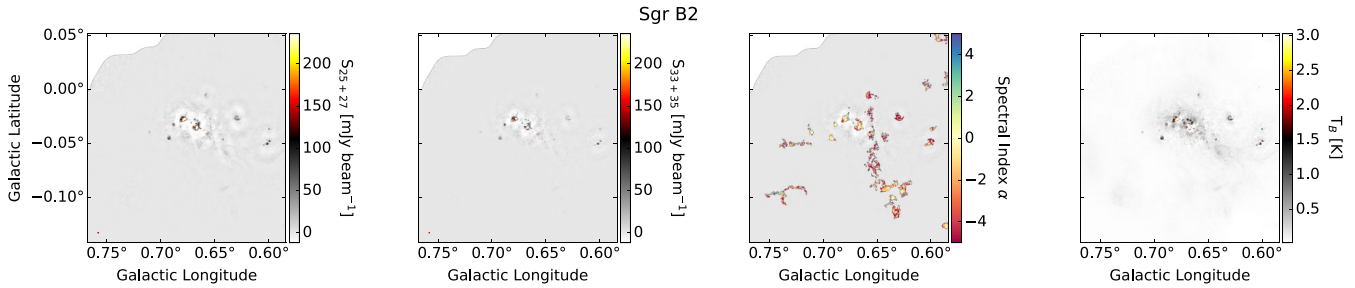


Figure A14. Like Fig. A1, but for the Sgr B2 region (see Fig. 13).

Downloaded from academic.oup.com/mnras/article/552/2/stag354/8875763 by Liverpool John Moores University user on 02 November 2026

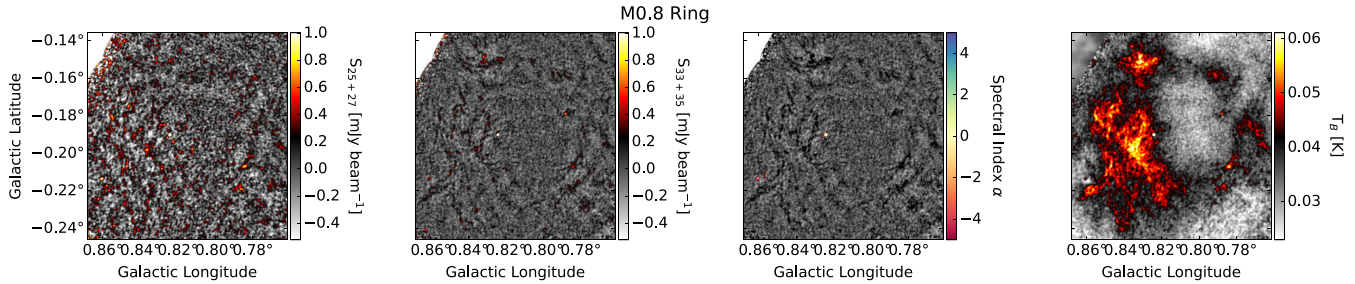


Figure A15. Like Fig. A1, but for the M. Nonhebel et al. (2024) ring region (see Fig. 13). Like the Brick (Fig. A11) and the southern dust ridge (Fig. A12), most of the cloud emission exists only on large angular scales and is resolved out. The rightmost panel convincingly demonstrates that the ring does indeed exist in dust, but is difficult to pick out in 12 m-only data.

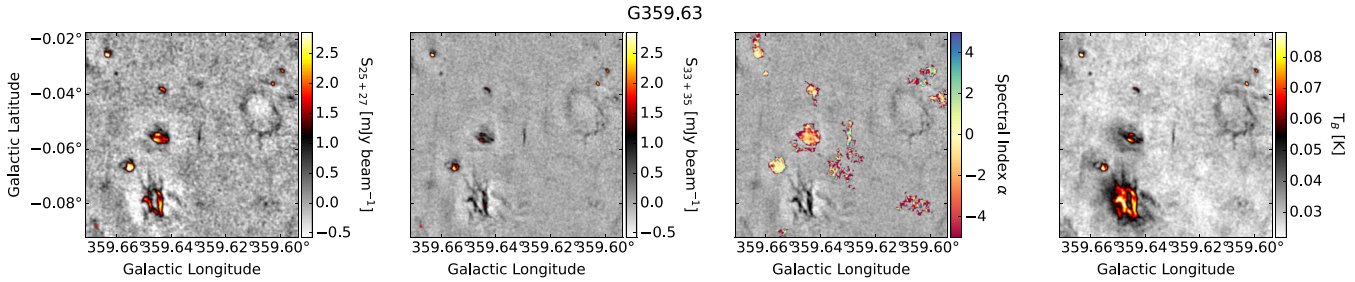


Figure A16. Like Fig. A1, but for the region G359.63 (see Fig. 13).

APPENDIX B: OBSERVATION METADATA TABLE

The full metadata table, Table B1, is presented here. The table includes the field name, time of each execution, the configuration, the PWV during the execution, the number of pointings in the scheduling block, the exposure time per mosaic pointing, and the expected resolution and largest angular scale.

Downloaded from academic.oup.com/mnras/article/552/2/stag354/8875763 by Liverpool John Moores University user on 02 November 2026

Table B1. 12 m observation metadata.

Centre	Field	Execution dates	EB ID	Configuration	PWV mm	Time min	N(P)	Res. ″	LAS ″
G359.448−00.183	ad	2022-01-05 19:14:51.991.	uid://A002/Xf49cca/Xde0f.	C-4	1.09	70.2	61	1.1	17
G359.463−00.090	aj	2022-05-09 09:34:09.882,	uid://A002/Xf8b429/X2c01„	C-3	0.35,	65.5,	147	1.6	22
		2022-05-09 07:19:14.47,	uid://A002/Xf8b429/X1ea4„		0.40,	65.5,			
		2022-05-08 09:39:43.05.	uid://A002/Xf89be2/Xe4fd.		1.68	65.4			
G359.511−00.166	ag	2022-05-16 05:15:44.	uid://A002/Xf8f6a9/X1912b„	C-3	1.12,	63.0,	140	1.3	19
		486,2022-05-15 10:21:36.497.	uid://A002/Xf8f6a9/X12db3.		0.38	62.8			
G359.543−00.041	e	2022-09-22 01:23:55.951,	uid://A002/Xfeb5e6/Xb30„	C-4	0.67,	65.1,	147	1.1	21
		2022-09-21 00:52:07.005.	uid://A002/Xfe90b7/Xbd5d.		0.96	65.1			
G359.590−00.121	ae	2022-05-13 07:23:53.702,	uid://A002/Xf8f6a9/X1947„	C-3	0.30,	64.2,	144	1.6	18
		2022-05-13 06:18:54.818.	uid://A002/Xf8f6a9/Xe40.		0.32	64.4			
G359.602−00.207	l	2022-05-16 06:22:59.613,	uid://A002/Xf8f6a9/X199a6„	C-3	1.24,	66.1,	149	1.2	18
		2022-05-15 09:14:38.483.	uid://A002/Xf8f6a9/X1251d.		0.38	66.3			
G359.622+00.003	t	2022-04-30 08:27:09.933,	uid://A002/Xf84513/Xd44b„	C-3	1.33,	60.7,	134	1.6	20
		2022-04-29 07:31:20.612.	uid://A002/Xf84513/X1a3e.		1.56	60.8			
G359.668−00.073	ap	2022-05-08 08:34:14.943,	uid://A002/Xf89be2/Xdba9„	C-3	1.82,	65.2,	146	1.6	19
		2022-05-08 07:29:00.701,	uid://A002/Xf89be2/Xd5f3„		1.68	,64.9,			
		2022-05-08 06:24:05.21.	uid://A002/Xf89be2/Xcf2b.		1.87	65.1			
G359.704+00.031	y	2022-01-25 15:02:47.947,	uid://A002/Xf53eeb/X3071„	C-3	7.35,	46.4,	74	1.5	18
		2022-01-22 15:59:25.572,	uid://A002/Xf531c1/X14f4„		5.84,	46.7,			
		2022-01-20 17:22:19.999.	uid://A002/Xf512ae/X64a7.		6.46	36.3			
G359.717−00.135	ab	2022-05-16 08:22:51.756,	uid://A002/Xf8f6a9/X1ab3f„	C-3	1.23,	55.0,	92	1.2	20
		2022-05-12 08:36:36.281.	uid://A002/Xf8d822/X6bdc.		0.86	54.8			
G359.748−00.025	q	2022-05-02 09:47:27.976,	uid://A002/Xf859f0/X43e5„	C-3	2.13,	64.9,	145	1.7	20
		2022-05-02 07:36:30.219,	uid://A002/Xf859f0/X3e35„		1.99,	64.5,			
		2022-04-29 08:36:06.955.	uid://A002/Xf84513/X23b6.		1.45	64.7			
G359.799−00.102	h	2022-05-22 08:58:23.814,	uid://A002/Xf96bbc/X3e74„	C-3	1.17,	65.0,	145	1.1	18
		2022-05-18 10:12:05.715.	uid://A002/Xf934b1/X30dd.		0.48	64.3			
G359.822+00.016	ai	2022-05-14 06:45:09.401,	uid://A002/Xf8f6a9/X85e2„	C-3	0.53,	69.9,	124	1.5	22
		2022-05-12 09:54:33.106.	uid://A002/Xf8d822/X728a.		0.78	69.7			
G359.874−00.055	p	2022-05-25 09:08:16.264,	uid://A002/Xf99390/X1b76„	C-4	0.58,	64.1,	144	1.1	17
		2022-05-25 08:03:12.566.	uid://A002/Xf99390/X12c7.		0.56	64.3			
G359.915−00.110	x	2022-06-12 06:27:16.623,	uid://A002/Xfa2f45/X258d„	C-3	-,	76.6,	31	13	91
		2022-05-15 10:18:23.434,	uid://A002/Xf8f6a9/X12c6a„		-,	73.9,			
		2022-05-15 09:04:25.963.	uid://A002/Xf8f6a9/X122d3.		-76.7				
G359.945+00.165	v	2022-09-01 03:02:48.482.	uid://A002/Xfdd416/Xfeb.	C-4	2.16	68.1	60	1.2	17
G359.952−00.007	aq	2022-04-06 10:23:42.108,	uid://A002/Xf73568/X1553„	C-4	-,	71.4,	52	12	76
		2022-04-06 08:27:11.543,	uid://A002/Xf73568/Xbfc„		-,	75.1,			
		2022-04-05 10:26:55.772,	uid://A002/Xf7294e/X2b09„		-,	74.9,			
		2022-01-27 15:24:49.778,	uid://A002/Xf53eeb/X10748„		-,	75.3,			
		2022-01-27 14:08:34.173,	uid://A002/Xf53eeb/Xfcbb„		-,	75.7,			
		2022-01-22 13:39:45.577,	uid://A002/Xf531c1/X545„		-,	75.7,			
		2022-01-08 14:19:32.254.	uid://A002/Xf49cca/X23d82.		-	76.1			
G359.972+00.089	am	2022-09-20 02:09:48.971,	uid://A002/Xfe90b7/X823e„	C-3	1.23,	65.4,	148	1.7	23

Downloaded from academic.oup.com/mnras/article/552/2/stag354/8875763 by Liverpool John Moores University user on 02 November 2026

Table B1 – *continued*

Centre	Field	Execution dates	EB ID	Configuration	PWV mm	Time min	N(P)	Res. ″	LAS ″
		2022-09-20 01:02:43.885.	uid://A002/Xfe90b7/X773a.		1.44	65.7			
G359.999−00.077	aa	2022-09-16 01:30:14.236,	uid://A002/Xfe62c1/Xa4d3„	C-3	0.50,	67.9,	120	1.3	19
		2022-09-15 01:25:32.273.	uid://A002/Xfe62c1/X2274.		0.37	68.1			
G000.029+00.041	r	2022-09-24 01:08:56.699,	uid://A002/Xfec857/X9f6„	C-3	0.52,	63.2,	141	1.7	21
		2022-09-23 01:09:43.032.	uid://A002/Xfeb5e6/X4fa5.		0.71	63.5			
G000.073+00.183	a	2022-08-27 03:03:13.83,	uid://A002/Xfd8c42/X15d3„	C-4	-,	75.5,	45	12	88
		2022-08-26 23:54:12.505,	uid://A002/Xfd8c42/X525„		-,	74.8,			
		2022-08-24 02:21:34.477.	uid://A002/Xfd6eb8/Xafb.		-	74.4			
G000.082−00.037	o	2022-09-30 00:44:54.677,	uid://A002/Xfef6d0/X269f„	C-3	0.45,	63.1,	141	1.7	23
		2022-09-28 23:24:31.463.	uid://A002/Xfef6d0/Xd8.		1.05	63.2			
G000.123−00.115	af	2022-09-17 02:00:32.793,	uid://A002/Xfe83cd/X125c„	C-3	1.07,	58.0,	130	1.7	20
		2022-09-17 00:48:37.892,	uid://A002/Xfe83cd/X286„		0.57,	58.1,			
		2022-09-16 22:21:51.301.	uid://A002/Xfe62c1/X10de7.		0.51	45.8			
G000.162+00.010	f	2022-09-28 00:20:09.967,	uid://A002/Xfee03e/X822c„	C-3	0.56,	62.7,	140	1.7	22
		2022-09-27 00:34:32.054.	uid://A002/Xfee03e/X2d13.		0.64	62.9			
G000.208−00.063	s	2022-09-26 23:26:43.52,	uid://A002/Xfee03e/X2787„	C-3	0.70,	61.6,	136	1.7	21
		2022-09-25 00:57:01.376.	uid://A002/Xfed4ee/X1e3.		0.66	61.2			
G000.286−00.019	c	2022-09-19 23:57:01.095,	uid://A002/Xfe90b7/X7016„	C-3	1.64,	64.7,	145	1.7	18
		2022-09-18 00:40:55.253.	uid://A002/Xfe90b7/X2ab.		2.34	64.5			
G000.300+00.063	ao	2022-01-25 16:00:32.766,	uid://A002/Xf53eeb/X323e„	C-3	7.06,	57.0,	95	1.6	19
		2022-01-22 16:56:41.945.	uid://A002/Xf531c1/X16b2.		5.89	57.1			
G000.323−00.089	d	2022-09-15 00:16:13.897,	uid://A002/Xfe62c1/X1871„	C-3	0.37,	68.1,	119	1.2	19
		2022-09-12 02:37:20.469.	uid://A002/Xfe3986/X9083.		2.06	67.4			
G000.367+00.029	as	2022-05-23 09:12:08.001,	uid://A002/Xf96bbc/Xbcc0„	C-3	0.84,	65.1,	146	1.1	19
		2022-05-22 10:18:49.464.	uid://A002/Xf96bbc/X41f2.		0.70	64.8			
G000.412−00.050	k	2022-08-29 03:46:11.755,	uid://A002/Xfda0c7/Xacb5„	C-4	3.55,	63.9,	143	1.1	18
		2022-05-27 09:23:02.46.	uid://A002/Xf99bb0/Xf742.		0.41	63.8			
G000.453+00.060	al	2022-05-13 08:17:48.547,	uid://A002/Xf8f6a9/X216b„	C-3	0.29,	48.6,	78	1.6	20
		2022-05-10 09:05:23.071.	uid://A002/Xf8b429/Xa4c5.		0.63	48.6			
G000.464−00.104	ac	2022-08-30 02:48:07.786.	uid://A002/Xfdb69b/X1e74.	C-4	1.80	66.1	58	1.2	16
G000.491−00.002	ar	2022-05-04 08:57:44.492,	uid://A002/Xf87688/X931„	C-3	0.46,	66.0,	148	1.6	18
		2022-05-02 08:42:30.42.	uid://A002/Xf859f0/X4107.		2.05	66.0			
G000.538−00.079	an	2022-05-14 07:53:05.542,	uid://A002/Xf8f6a9/X8d0c„	C-3	0.50,	62.0,	137	1.5	21
		2022-05-13 10:21:58.756.	uid://A002/Xf8f6a9/X2f1d.		0.30	61.6			
G000.569+00.044	z	2022-05-14 09:28:16.65,	uid://A002/Xf8f6a9/X9732„	C-3	0.50,	61.4,	136	1.6	19
		2022-05-13 09:20:16.997.	uid://A002/Xf8f6a9/X269f.		0.30	61.6			
G000.601−00.131	u	2022-09-03 03:19:48.814.	uid://A002/Xfddca6/X8451.	C-4	0.60	44.2	36	1.2	18

Downloaded from academic.oup.com/mnras/article/552/2/stag354/8875763 by Liverpool John Moores University user on 02 November 2026

Table B1 – *continued*

Centre	Field	Execution dates	EB ID	Configuration	PWV mm	Time min	N(P)	Res. ″	LAS ″
G000.616−00.033	b	2022-05-26 09:44:28.024,	uid://A002/Xf99bb0/X4ae1„	C-4	0.77,	65.2,	147	1.1	18
		2022-05-26 08:38:20.722,	uid://A002/Xf99bb0/X3f39„		0.70,	65.3,			
		2022-05-26 04:46:55.553.	uid://A002/Xf99bb0/X2491.		0.53	65.7			
G000.637+00.070	ak	2022-04-07 08:35:00.62,	uid://A002/Xf73ead/X1d0f„	C-2	-,	64.9,	25	12	92
		2022-04-06 12:46:15.491,	uid://A002/Xf73568/X1f60„		-,	62.8,			
		2022-04-06 11:43:25.533.	uid://A002/Xf73568/X1c47.		-	65.0			
G000.665−00.111	i	2022-05-16 09:28:22.185,	uid://A002/Xf8f6a9/X1b140„	C-3	1.18,	64.4,	144	1.2	18
		2022-05-16 07:27:40.23.	uid://A002/Xf8f6a9/X1a382.		1.30	64.6			
G000.692+00.005	m	2022-01-27 15:01:24.852,	uid://A002/Xf53eeb/X1055f„	C-3	8.34,	65.2,	112	1.6	20
		2022-01-26 15:28:51.686.	uid://A002/Xf53eeb/Xa0e8.		5.72	65.8			
G000.715−00.180	w	2022-05-16 10:36:44.557,	uid://A002/Xf8f6a9/X1b8a0„	C-3	1.13,	67.4,	118	1.4	20
		2022-05-10 08:03:41.495.	uid://A002/Xf8b429/X991b.		0.60	67.7			
G000.741−00.064	j	2022-05-04 11:22:09.805,	uid://A002/Xf87688/Xf8e„	C-3	0.35,	63.0,	141	1.7	22
		2022-05-04 10:01:48.267.	uid://A002/Xf87688/Xc13.		0.41	63.2			
G000.774−00.244	n	2022-08-29 02:41:37.35.	uid://A002/Xfda0c7/Xa597.	C-4	3.44	60.1	51	1.1	16
G000.792−00.142	g	2022-05-15 07:15:22.553,	uid://A002/Xf8f6a9/X113a4„	C-3	0.47,	63.5,	141	1.3	21
		2022-05-14 10:34:49.257.	uid://A002/Xf8f6a9/X9e67.		0.50	63.1			
G000.835−00.215	ah	2022-08-30 22:57:42.302,	uid://A002/Xfdb69b/X7a3c„	C-4	-,	79.0,	49	13	92
		2022-08-30 03:10:02.834,	uid://A002/Xfdb69b/X20cc„		-,	76.4,			
		2022-08-29 03:30:50.762,	uid://A002/Xfda0c7/Xa983„		-,	76.6,			
		2022-08-29 02:12:44.32.	uid://A002/Xfda0c7/X9fc0.		-	78.4			

Note. The *Time* column gives the execution time of each execution block. The *PWV* is the median of the water column in the `ASDM_CALWVR` table. *Res.* is the resolution in arcseconds. *N(P)* is the number of pointings.

Downloaded from academic.oup.com/mnras/article/552/2/stag354/8875763 by Liverpool John Moores University user on 02 November 2026

APPENDIX C: CONTINUUM DATA SUMMARY TABLE

A summary of the continuum imaging is reported in Table C1. This table reports the properties of the individual continuum images that comprise the full ACES mosaic. The naming convention is given in Section D.

APPENDIX D: DATA RELEASE SUMMARY

The data products from the ACES survey follow a uniform naming convention. The filenames for the data products presented in this paper (continuum) can be constructed using the templates described below, in conjunction with the information provided in Table B1.

Table C1. Continuum Data Summary.

Region	θ_{maj} $''$	θ_{min} $''$	BPA $^\circ$	Robust	SPWs	S_{peak} mJy beam^{-1}	σ_{MAD} mJy beam^{-1}	$T_{B,peak}$ K	$\sigma_{MAD,mK}$ mK
G359.448−00.183	1.9	1.1	−75	r1.0	25,27	3.2	0.093	0.24	6.9
G359.448−00.183	1.7	0.98	−75	r1.0	33,35	2.5	0.063	0.19	4.8
G359.448−00.183	1.7	1.0	−75	r1.0	all	2.8	0.068	0.20	5.0
G359.463−00.090	2.2	1.6	86	r0.0	25,27	14	0.17	0.67	7.8
G359.463−00.090	1.8	1.4	86	r0.0	33,35	19	0.095	0.91	4.7
G359.463−00.090	1.9	1.5	86	r0.0	all	17	0.094	0.76	4.4
G359.511−00.166	1.8	1.4	−79	r0.5	25,27	1.3	0.11	0.086	7.4
G359.511−00.166	1.5	1.1	−78	r0.5	33,35	0.71	0.063	0.052	4.6
G359.511−00.166	1.6	1.2	−79	r0.5	all	0.79	0.066	0.054	4.6
G359.543−00.041	2.6	1.6	90	r0.0	25,27	2.5	0.18	0.099	7.0
G359.543−00.041	2.0	1.4	89	r0.0	33,35	3.5	0.11	0.16	4.8
G359.543−00.041	2.1	1.4	90	r0.0	all	3.1	0.10	0.13	4.5
G359.590−00.121	2.1	1.7	82	r0.5	25,27	0.69	0.13	0.031	5.6
G359.590−00.121	1.8	1.4	83	r0.5	33,35	0.56	0.061	0.027	3.0
G359.590−00.121	1.9	1.5	83	r0.5	all	0.49	0.064	0.023	3.0
G359.602−00.207	1.6	1.4	−77	r0.5	25,27	12	0.14	0.86	11
G359.602−00.207	1.3	1.2	−74	r0.5	33,35	15	0.080	1.2	6.1
G359.602−00.207	1.4	1.2	−76	r0.5	all	13	0.080	0.99	5.9
G359.622+00.003	2.2	1.8	74	r0.5	25,27	1.4	0.12	0.060	5.0
G359.622+00.003	1.8	1.5	73	r0.5	33,35	2.1	0.077	0.093	3.4
G359.622+00.003	1.9	1.6	73	r0.5	all	1.9	0.079	0.081	3.4
G359.668−00.073	2.1	1.7	79	r0.5	25,27	2.5	0.12	0.11	5.5
G359.668−00.073	1.8	1.4	80	r0.5	33,35	1.9	0.075	0.094	3.6
G359.668−00.073	1.9	1.5	80	r0.5	all	2.1	0.080	0.097	3.6
G359.704+00.031	2.1	1.6	−86	r0.5	25,27	0.66	0.11	0.032	5.3
G359.704+00.031	1.7	1.3	−86	r0.5	33,35	0.69	0.067	0.037	3.6
G359.704+00.031	1.9	1.4	−86	r0.5	all	0.63	0.068	0.032	3.5
G359.717−00.135	1.9	1.6	−87	r0.5	25,27	3.6	0.095	0.20	5.3
G359.717−00.135	1.5	1.3	−86	r0.5	33,35	2.9	0.064	0.17	3.9
G359.717−00.135	1.6	1.4	−84	r0.5	all	3.1	0.064	0.17	3.7
G359.748−00.025	2.3	1.7	88	r0.5	25,27	4.4	0.12	0.18	5.1
G359.748−00.025	1.9	1.5	89	r0.5	33,35	3.5	0.068	0.16	3.1
G359.748−00.025	2.0	1.5	89	r0.5	all	3.7	0.075	0.16	3.2
G359.799−00.102	1.6	1.2	−83	r0.5	25,27	1.5	0.096	0.13	8.1
G359.799−00.102	1.4	1.0	−82	r0.5	33,35	1.0	0.061	0.093	5.6
G359.799−00.102	1.4	1.0	−82	r0.5	all	1.2	0.064	0.11	5.6
G359.822+00.016	2.4	1.6	78	r0.5	25,27	8.3	0.13	0.34	5.3
G359.822+00.016	2.0	1.4	77	r0.5	33,35	9.3	0.070	0.42	3.2
G359.822+00.016	2.1	1.4	78	r0.5	all	8.9	0.074	0.38	3.2
G359.874−00.055	1.7	1.3	85	r1.0	25,27	9.6	0.16	0.70	12
G359.874−00.055	1.5	1.1	87	r1.0	33,35	14	0.096	1.0	7.0
G359.874−00.055	1.5	1.2	86	r1.0	all	12	0.11	0.86	7.6
G359.915−00.108	2.5	1.7	−88	r0.5	25,27	1.3	0.11	0.048	4.3
G359.915−00.108	2.1	1.4	−86	r0.5	33,35	0.63	0.075	0.027	3.2
G359.915−00.108	2.2	1.5	−87	r0.5	all	0.59	0.079	0.024	3.2
G359.945+00.165	1.8	1.1	−80	r0.5	25,27	6.0	0.11	0.48	9.1
G359.945+00.165	1.5	0.95	−79	r0.5	33,35	4.1	0.045	0.36	3.9
G359.945+00.165	1.6	1.0	−79	r0.5	all	5.0	0.067	0.41	5.5
G359.952−00.007	1.6	1.3	−84	r0.5	25,27	2400	0.26	190	20
G359.952−00.007	1.4	1.1	−82	r0.5	33,35	2600	0.13	220	11
G359.952−00.007	1.4	1.1	−82	r0.5	all	2500	0.15	200	12
G359.999−00.077	1.8	1.5	−71	r0.5	25,27	33	0.17	2.0	10

Downloaded from academic.oup.com/mnras/article/552/2/stag354/8875763 by Liverpool John Moores University user on 02 November 2026

Table C1 – *continued*

Region	θ_{maj} $''$	θ_{min} $''$	BPA $^\circ$	Robust	SPWs	S_{peak} mJy beam^{-1}	σ_{MAD} mJy beam^{-1}	$T_{B,peak}$ K	$\sigma_{MAD,mK}$ mK
G359.999−00.077	1.5	1.3	−61	r0.5	33,35	27	0.095	1.7	6.0
G359.999−00.077	1.6	1.3	−63	r0.5	all	28	0.11	1.7	6.6
G000.029+00.041	2.8	1.5	−85	r0.0	25,27	44	0.23	1.7	9.0
G000.029+00.041	2.1	1.3	−85	r0.0	33,35	33	0.13	1.5	5.7
G000.029+00.041	2.3	1.4	−85	r0.0	all	37	0.15	1.5	6.0
G000.073+00.184	1.6	1.1	−76	r0.5	25,27	0.56	0.095	0.050	8.4
G000.073+00.184	1.4	0.96	−73	r0.5	33,35	0.67	0.057	0.064	5.4
G000.073+00.184	1.4	1.0	−74	r0.5	all	0.74	0.059	0.067	5.3
G000.082−00.037	2.5	1.7	88	r0.0	25,27	21	0.21	0.81	8.4
G000.082−00.037	1.9	1.5	87	r0.0	33,35	17	0.13	0.75	5.8
G000.082−00.037	2.0	1.5	87	r0.0	all	18	0.15	0.75	6.2
G000.123−00.115	2.5	1.5	−90	r0.0	25,27	35	0.19	1.5	7.9
G000.123−00.115	2.0	1.3	88	r0.0	33,35	30	0.097	1.5	4.7
G000.123−00.115	2.1	1.3	88	r0.0	all	32	0.11	1.4	5.1
G000.162+00.010	2.6	1.6	−90	r0.0	25,27	22	0.27	0.90	11
G000.162+00.010	2.0	1.3	89	r0.0	33,35	17	0.14	0.83	6.7
G000.162+00.010	2.2	1.4	89	r0.0	all	19	0.17	0.83	7.7
G000.208−00.063	2.3	1.6	88	r0.0	25,27	8.1	0.21	0.36	9.4
G000.208−00.063	1.8	1.4	85	r0.0	33,35	5.8	0.13	0.27	6.2
G000.208−00.063	2.0	1.5	86	r0.0	all	6.4	0.15	0.28	6.5
G000.286−00.019	2.5	1.6	87	r0.0	25,27	4.5	0.19	0.19	7.9
G000.286−00.019	1.9	1.3	86	r0.0	33,35	3.4	0.11	0.17	5.6
G000.286−00.019	2.1	1.4	86	r0.0	all	3.6	0.12	0.16	5.3
G000.300+00.063	2.4	1.5	−87	r0.5	25,27	6.5	0.15	0.29	6.7
G000.300+00.063	2.0	1.3	−88	r0.5	33,35	5.8	0.093	0.28	4.4
G000.300+00.063	2.1	1.4	−87	r0.5	all	6.2	0.094	0.28	4.2
G000.323−00.089	1.8	1.3	−63	r0.5	25,27	5.8	0.12	0.43	8.7
G000.323−00.089	1.5	1.1	−61	r0.5	33,35	4.1	0.075	0.32	5.9
G000.323−00.089	1.5	1.1	−61	r0.5	all	4.7	0.076	0.35	5.7
G000.367+00.029	1.8	1.1	−74	r0.5	25,27	30	0.16	2.4	13
G000.367+00.029	1.5	0.94	−74	r0.5	33,35	43	0.089	3.7	7.8
G000.367+00.029	1.6	0.99	−74	r0.5	all	37	0.089	3.1	7.4
G000.412−00.050	1.8	1.0	−79	r0.5	25,27	4.7	0.11	0.41	9.5
G000.412−00.050	1.5	0.88	−78	r0.5	33,35	3.6	0.078	0.34	7.3
G000.412−00.050	1.6	0.92	−78	r0.5	all	4.0	0.081	0.35	7.2
G000.453+00.060	2.5	1.7	88	r0.5	25,27	1.4	0.098	0.057	3.9
G000.453+00.060	2.0	1.4	89	r0.5	33,35	1.3	0.064	0.057	2.8
G000.453+00.060	2.2	1.5	89	r0.5	all	1.3	0.067	0.055	2.7
G000.464−00.104	1.7	1.1	−77	r0.5	25,27	1.7	0.089	0.15	7.7
G000.464−00.104	1.4	0.93	−76	r0.5	33,35	0.82	0.068	0.077	6.4
G000.464−00.104	1.5	0.98	−77	r0.5	all	1.1	0.068	0.10	6.1
G000.491−00.002	2.2	1.7	84	r0.5	25,27	9.8	0.18	0.43	7.9
G000.491−00.002	1.8	1.4	87	r0.5	33,35	11	0.11	0.51	5.1
G000.491−00.002	1.9	1.5	87	r0.5	all	9.2	0.11	0.42	5.2
G000.538−00.079	2.4	1.6	82	r0.5	25,27	11	0.18	0.49	7.8
G000.538−00.079	1.9	1.4	80	r0.5	33,35	8.7	0.11	0.40	5.2
G000.538−00.079	2.0	1.4	81	r0.5	all	9.6	0.12	0.42	5.4
G000.569+00.044	2.4	1.5	81	r0.0	25,27	1.9	0.13	0.087	6.0
G000.569+00.044	1.9	1.3	78	r0.0	33,35	1.8	0.082	0.092	4.2
G000.569+00.044	2.0	1.3	79	r0.0	all	1.6	0.080	0.074	3.8
G000.601−00.131	1.9	1.1	−75	r0.5	25,27	0.87	0.091	0.065	6.8
G000.601−00.131	1.6	0.97	−75	r0.5	33,35	0.58	0.054	0.047	4.4
G000.601−00.131	1.7	1.0	−75	r0.5	all	0.62	0.054	0.047	4.1
G000.616−00.033	1.6	1.2	87	r0.5	25,27	2600	0.27	230	23
G000.616−00.033	1.3	1.0	89	r0.5	33,35	2500	0.14	230	13
G000.616−00.033	1.4	1.1	88	r0.5	all	2500	0.16	220	15
G000.637+00.068	2.3	1.9	78	r0.5	25,27	0.52	0.094	0.019	3.5
G000.637+00.068	1.9	1.6	80	r0.5	33,35	0.33	0.061	0.014	2.6
G000.637+00.068	2.0	1.6	79	r0.5	all	0.39	0.064	0.016	2.6
G000.665−00.111	1.6	1.4	−65	r0.5	25,27	5.2	0.15	0.37	11
G000.665−00.111	1.4	1.2	−63	r0.5	33,35	2.7	0.090	0.21	7.0
G000.665−00.111	1.4	1.2	−64	r0.5	all	3.3	0.098	0.24	7.2
G000.692+00.005	2.2	1.7	81	r0.0	25,27	1900	0.27	86	12

Downloaded from academic.oup.com/mnras/article/552/2/stag354/8875763 by Liverpool John Moores University user on 02 November 2026

Table C1 – *continued*

Region	θ_{maj} $''$	θ_{min} $''$	BPA $^\circ$	Robust	SPWs	S_{peak} mJy beam^{-1}	σ_{MAD} mJy beam^{-1}	$T_{B,peak}$ K	$\sigma_{MAD,mK}$ mK
G000.692+00.005	1.8	1.4	82	r0.0	33,35	1700	0.15	85	7.7
G000.692+00.005	1.9	1.5	82	r0.0	all	1700	0.16	82	7.5
G000.715−00.180	2.3	1.6	−82	r0.5	25,27	2.1	0.10	0.092	4.4
G000.715−00.180	1.9	1.3	−79	r0.5	33,35	1.3	0.067	0.066	3.3
G000.715−00.180	2.0	1.4	−80	r0.5	all	1.6	0.068	0.074	3.1
G000.741−00.064	2.6	1.5	−87	r0.0	25,27	71	0.22	3.0	9.1
G000.741−00.064	2.1	1.2	−87	r0.0	33,35	35	0.13	1.7	6.1
G000.741−00.064	2.2	1.3	−87	r0.0	all	49	0.12	2.1	5.4
G000.774−00.244	1.8	1.1	−80	r1.0	25,27	2.4	0.093	0.20	7.7
G000.774−00.244	1.6	0.97	−79	r1.0	33,35	3.8	0.070	0.31	5.7
G000.774−00.244	1.6	1.0	−79	r1.0	all	3.3	0.072	0.26	5.8
G000.792−00.142	1.9	1.4	86	r0.5	25,27	0.67	0.12	0.040	7.3
G000.792−00.142	1.6	1.2	86	r0.5	33,35	0.47	0.069	0.031	4.5
G000.792−00.142	1.7	1.3	87	r0.5	all	0.48	0.071	0.029	4.4
G000.835−00.216	1.8	1.1	−72	r0.5	25,27	30	0.12	2.5	9.6
G000.835−00.216	1.5	0.95	−71	r0.5	33,35	30	0.066	2.6	5.8
G000.835−00.216	1.5	1.0	−71	r0.5	all	30	0.066	2.5	5.5

The following subsections are divided according to different product types which occur at the Member ObsUnitSet (MOUS) and Group ObsUnitSet (GOUS) levels.[12]

D1 Member-level products (12 m)

We release all continuum images for the 45 ACES regions. These are member-level products, and correspond to the images for the 12 m array for each field prior to mosaicing. As described in Section 3.3, for each field, we produce three images as outlined in Tables D2 and D1.

Following the requirements of the ASA, the filename template is:

`member.uid___A001_{mous-id}.lp_slongmore.{field_coords}.{array}.{frqcen}_{bw}.cont.{contsuffix}.fits`

The placeholder template components should be replaced as follows:

(i) {**mous-id**}: The MOUS ID for a given field, as listed in Table D1.
(ii) {**field_coords**}: The central coordinates of the field from Table D1 (e.g. `G000.073+0.184`).
(iii) {**array**}: The ALMA array. For the continuum data, only `12 m` is distributed.
(iv) {**frqcen**}: The frequency centre, which corresponds to the spectral windows used (see Table D2):
(v) {**bw**}: The bandwidth, which also corresponds to the spectral windows used (see Table D2):
(vi) {**contsuffix**}: The continuum file name suffix. This is in two parts, the Taylor term (either `tt0` or `tt1`) and the image type. Distributed products include `image`, `image.pbcor`, `model`, and `residual`.

For example,

`member.uid___A001_X15b4_X4b.lp_slongmore.G000.64+00.07.12m.cont.99.6GHz_bw3.8GHz.tt1.residual.fits`

is the Taylor-term 1 (slope) residual image for the high-frequency (spw33+35) image of G0.64+0.07, field `ak`.

D2 Group-level products (Full CMZ mosaics)

We release the full, contiguous mosaics covering the entire ACES footprint. Since these result from the combination of many MOUSs, the full mosaics are at the group level.

The filename template for the full mosaic cubes and associated products is:

`group.uid___A001_X1590_X30a9.lp_slongmore.cmz_mosaic.{arrays}.cont.{frqcen}_{bw}.{suffix}`

Where the template components are:

(i) {**arrays**} can be either `12m` or `12mGBT-MUSTANG`
(ii) {**frqcen**} and {**bw**} are as described in Section D1
(iii) {**suffix**} defines the specific data product. Products released with this paper are, for each spectral window set:

(a) `pbcor.fits`: primary beam corrected image mosaic.
(b) `maskedrms.pbcor.fits`: the corresponding uncertainty map.

Additionally, there are `alpha` maps that only correspond to the aggregate bandwidth `93.7GHz_bw4.7GHz`

(a) `alpha.fits`:
(b) `alpha.maskedrms.fits`:
(c) `alpha_manual.fits`:
(d) `alpha_manual.maskedrms.fits`:

An example for the low-frequency composite 12m-only image is:

`group.uid___A001_X1590_X30a9.lp_slongmore.cmz_mosaic.12m.cont.86.6GHz_bw1.0GHz.pbcor.fits`

[12]For a description of ALMA project structures and naming conventions, please refer to Section 2 of the Cycle 9 QA2 guide: https://almascience.eso.org/documents-and-tools/cycle9/alma-qa2-data-products-for-cycle-9

[1]*Department of Astronomy, University of Florida, PO Box 112055, Gainesville, FL 32611, USA*
[2]*UK ALMA Regional Centre Node, Jodrell Bank Centre for Astrophysics, The University of Manchester, Manchester M13 9PL, UK*

Downloaded from academic.oup.com/mnras/article/552/2/stag354/8875763 by Liverpool John Moores University user on 02 November 2026

Table D1. Field information with central coordinates and MOUS IDs.

Central Coordinates	Field ID	12 m MOUS ID	7 m MOUS ID	TP MOUS ID
G359.448−0.183	ad	X15a0_X14e	X15a0_X150	X15a0_X152
G359.463−0.090	aj	X15a0_X172	X15b4_X47	X15b4_X49
G359.511−0.166	ag	X15a0_X160	X15a0_X162	X15a0_X164
G359.543−0.041	e	X15a0_Xb8	X15b4_X39	X15a0_Xbc
G359.590−0.121	ae	X15a0_X154	X15a0_X156	X15a0_X158
G359.602−0.207	l	X15a0_Xe2	X15a0_Xe4	X15a0_Xe6
G359.622+0.003	t	X15a0_X112	X15a0_X114	X15a0_X116
G359.668−0.073	ap	X15a0_X196	X15a0_X198	X3577_X6c5
G359.704+0.031	y	X15a0_X130	X15a0_X132	X15a0_X134
G359.717−0.135	ab	X15a0_X142	X15a0_X144	X15a0_X146
G359.748−0.025	q	X15a0_X100	X15a0_X102	X15a0_X104
G359.799−0.102	h	X15a0_Xca	X15a0_Xcc	X15a0_Xce
G359.822+0.016	ai	X15a0_X16c	X15a0_X16e	X15a0_X170
G359.874−0.055	p	X15a0_Xfa	X15a0_Xfc	X15a0_Xfe
G359.915−0.108	x	X15a0_X12a	X15a0_X12c	X15a0_X12e
G359.945+0.165	v	X15a0_X11e	X15a0_X120	X15a0_X122
G359.952−0.007	aq	X15a0_X19c	X15a0_X19e	X15a0_X1a0
G359.972+0.089	am	X15a0_X184	X15a0_X186	X15a0_X188
G359.999−0.077	aa	X15a0_X13c	X15a0_X13e	X15a0_X140
G000.029+0.041	r	X15a0_X106	X15a0_X108	X15a0_X10a
G000.073+0.184	a	X1590_X30aa	X1590_X30ac	X1590_X30ae
G000.082−0.037	o	X15a0_Xf4	X15a0_Xf6	X15a0_Xf8
G000.123−0.115	af	X15a0_X15a	X15a0_X15c	X15a0_X15e
G000.162+0.010	f	X15a0_Xbe	X15a0_Xc0	X15a0_Xc2
G000.208−0.063	s	X15a0_X10c	X15a0_X10e	X15a0_X110
G000.286−0.019	c	X15a0_Xac	X15a0_Xae	X15a0_Xb0
G000.300+0.063	ao	X15a0_X190	X15a0_X192	X15a0_X194
G000.323−0.089	d	X15a0_Xb2	X15a0_Xb4	X15a0_Xb6
G000.367+0.029	as	X15a0_X1a8	X15a0_X1aa	X15a0_X1ac
G000.412−0.050	k	X15a0_Xdc	X15a0_Xde	X15a0_Xe0
G000.453+0.060	al	X15a0_X17e	X15a0_X180	X15a0_X182
G000.464−0.104	ac	X15a0_X148	X15a0_X14a	X15a0_X14c
G000.491−0.002	ar	X15a0_X1a2	X15b4_X4f	X15a0_X1a6
G000.538−0.079	an	X15a0_X18a	X15a0_X18c	X15a0_X18e
G000.569+0.044	z	X15a0_X136	X15a9_X12d3	X15a0_X13a
G000.601−0.131	u	X15a0_X118	X15a0_X11a	X15a0_X11c
G000.616−0.033	b	X15a0_Xa6	X15b4_X37	X15a0_Xaa
G000.637+0.068	ak	X15b4_X4b	X15a9_X12d5	X15b4_X4d
G000.665−0.111	i	X15a0_Xd0	X15b4_Xc5	X15a0_Xd4
G000.692+0.005	m	X15b4_X41	X15b4_X43	X15b4_X45
G000.715−0.180	w	X15a0_X124	X15a0_X126	X15a0_X128
G000.741−0.064	j	X15b4_X3d	X15a0_Xd8	X15b4_X3f
G000.774−0.244	n	X15a0_Xee	X15a0_Xf0	X15a0_Xf2
G000.792−0.142	g	X15a0_Xc4	X15a0_Xc6	X15a0_Xc8
G000.835−0.216	ah	X15a0_X166	X15a0_X168	X15a0_X16a

Note. Only the 12 m MOUS UIDs are used for file naming in this paper; the 7 m and TP data set IDs are included for reference.

Table D2. Image file name convention information.

frqcen	bw	SPWs
99.6GHz	bw3.8GHz	33,35
93.7GHz	bw4.7GHz	25,27,33,35
86.6GHz	bw1.0GHz	25,27

[3]*European Southern Observatory (ESO), Karl-Schwarzschild-Straße 2, D-85748 Garching, Germany*
[4]*Shanghai Astronomical Observatory, Chinese Academy of Sciences, 80 Nandan Road, Shanghai 200030, P. R. China*
[5]*State Key Laboratory of Radio Astronomy and Technology, A20 Datun Road, Chaoyang District, Beijing, 100101, P. R. China*
[6]*Institut de Ciències de l'Espai (ICE), CSIC, Campus UAB, Carrer de Can Magrans s/n, E-08193 Bellaterra, Barcelona, Spain*
[7]*Institut d'Estudis Espacials de Catalunya (IEEC), E-08860 Castelldefels, Barcelona, Spain*
[8]*Max-Planck-Institut für extraterrestrische Physik, Gießenbachstraße 1, D-85748 Garching bei München, Germany*
[9]*University of Maryland, Department of Astronomy, College Park, MD 20742-2421, USA*
[10]*National Astronomical Observatory of Japan, 2-21-1 Osawa, Mitaka, Tokyo 181-8588, Japan*
[11]*Center for Astrophysics | Harvard & Smithsonian, 60 Garden Street, Cambridge, MA 02138, USA*
[12]*National Radio Astronomy Observatory, 520 Edgemont Road, Charlottesville, VA 22903, USA*

Downloaded from academic.oup.com/mnras/article/552/2/stag354/8875763 by Liverpool John Moores University user on 02 November 2026

[13]*Department of Physics and Astronomy, University of Kansas, 1251 Wescoe Hall Drive, Lawrence, KS 66045, USA*
[14]*Center for Astrophysics and Space Astronomy, Department of Astrophysical and Planetary Sciences, University of Colorado, Boulder, CO 80389, USA*
[15]*Centro de Astrobiología (CAB), CSIC-INTA, Carretera de Ajalvir km 4, 28850 Torrejón de Ardoz, Madrid, Spain*
[16]*Instituto de Astronomía, Universidad Católica del Norte, Av. Angamos 0610, Antofagasta, Chile*
[17]*Chinese Academy of Sciences South America Center for Astronomy, National Astronomical Observatories, CAS, Beijing 100101, China*
[18]*Astrophysics Research Institute, Liverpool John Moores University, 146 Brownlow Hill, Liverpool L3 5RF, UK*
[19]*Max Planck Institute for Astronomy, Königstuhl 17, D-69117 Heidelberg, Germany*
[20]*Universität Heidelberg, Zentrum für Astronomie, Institut für Theoretische Astrophysik, Albert-Ueberle-Str 2, D-69120 Heidelberg, Germany*
[21]*Universität Heidelberg, Interdisziplinäres Zentrum für Wissenschaftliches Rechnen, Im Neuenheimer Feld 225, D-69120 Heidelberg, Germany*
[22]*Elizabeth S. and Richard M. Cashin Fellow at the Radcliffe Institute for Advanced Studies at Harvard University, 10 Garden Street, Cambridge, MA 02138, USA*
[23]*Department of Physics and Astronomy, University of Pennsylvania, 209 S. 33rd Street, Philadelphia, PA 19104, USA*
[24]*Cosmic Origins Of Life (COOL) Research DAO, https://coolresearch.io*
[25]*Instituto de Astrofísica de Andalucía, CSIC, Glorieta de la Astronomía s/n, E-18008 Granada, Spain*
[26]*Instituto de Física Fundamental (CSIC), Calle Serrano 121-123, E-28006, Madrid, Spain*
[27]*Department of Astronomy, University of Massachusetts, Amherst, MA 01003, USA*
[28]*Kavli Institute for Astronomy and Astrophysics, Peking University, Beijing 100871, P. R. China*
[29]*Department of Astronomy, School of Physics, Peking University, Beijing 100871, P. R. China*
[30]*Department of Physics, University of Connecticut, 196A Auditorium Road, Unit 3046, Storrs, CT 06269, USA*
[31]*Academia Sinica Institute of Astronomy and Astrophysics, Astronomy-Mathematics Building, AS/NTU No.1, Sec. 4, Roosevelt Rd, Taipei 10617, Taiwan*
[32]*Space, Earth and Environment Department, Chalmers University of Technology, SE-412 96 Gothenburg, Sweden*
[33]*Como Lake centre for AstroPhysics (CLAP), DiSAT, Università dell'Insubria, via Valleggio 11, I-22100 Como, Italy*
[34]*Institute of Physics, Laboratory for Galaxy Evolution and Spectral Modelling, EPFL, Observatoire de Sauverny, Chemin Pegasi 51, I-1290 Versoix, Switzerland*
[35]*Observatorio Astronómico de Quito, Observatorio Astronómico Nacional, Escuela Politécnica Nacional, 170403 Quito, Ecuador*
[36]*INAF Arcetri Astrophysical Observatory, Largo Enrico Fermi 5, Firenze, I-50125, Italy*
[37]*Jodrell Bank Centre for Astrophysics, The University of Manchester, Manchester M13 9PL, UK*
[38]*Dept. of Astronomy, University of Virginia, Charlottesville, Virginia 22904, USA*
[39]*Leiden Observatory, Leiden University, PO Box 9513, NL-2300 RA Leiden, the Netherlands*
[40]*Research School of Astronomy and Astrophysics, Australian National University, Canberra, ACT 2611, Australia*
[41]*Institute for Advanced Study, 1 Einstein Drive, Princeton, NJ 08540, USA*
[42]*Department of Physics and Astronomy, University College London, Gower Street, London WC1E 6BT, UK*
[43]*Astronomisches Rechen-Institut, Zentrum für Astronomie der Universität Heidelberg, Mönchhofstraße 12-14, D-69120 Heidelberg, Germany*
[44]*European Southern Observatory, Alonso de Córdova, 3107, Vitacura, Santiago 763-0355, Chile*
[45]*Joint ALMA Observatory, Alonso de Córdova, 3107, Vitacura, Santiago 763-0355, Chile*
[46]*Institute for Research in Fundamental Sciences (IPM), School of Astronomy, P.O. Box 19395-5531, Tehran, Iran*
[47]*School of Astronomy and Space Science, Nanjing University, 163 Xianlin Avenue, Nanjing 210023, P. R. China*
[48]*Key Laboratory of Modern Astronomy and Astrophysics (Nanjing University), Ministry of Education, Nanjing 210023, P. R. China*
[49]*Department of Physics, Villanova University, 800 E. Lancaster Avenue, Villanova, PA 19085, USA*
[50]*Haystack Observatory, Massachusetts Institute of Technology, 99 Millstone Road, Westford, MA 01886, USA*
[51]*Departamento de Astronomía, Universidad de La Serena, Raúl Bitrán 1305, La Serena, Chile*
[52]*Green Bank Observatory, PO Box 2, Green Bank, WV 24944, USA*
[53]*Institute of Astronomy, The University of Tokyo, Mitaka, Tokyo 181-0015, Japan*
[54]*Department of Physics, Aberystwyth University, Ceredigion, Cymru SY23 3BZ, UK*

This paper has been typeset from a TEX/LATEX file prepared by the author.

Downloaded from academic.oup.com/mnras/article/552/2/stag354/8875763 by Liverpool John Moores University user on 02 November 2026

© The Author(s) 2026.
Published by Oxford University Press on behalf of Royal Astronomical Society. This is an Open Access article distributed under the terms of the Creative Commons Attribution License (https://creativecommons.org/licenses/by/4.0/), which permits unrestricted reuse, distribution, and reproduction in any medium, provided the original work is properly cited.